Mineralogical and geochemical changes in subsurface shales straddling the Ordovician–Silurian boundary in the eastern Kufra Basin, Libya

Guido Meinhold[1,2,3*], James Howard[1,4], Yousef Abutarruma[5], Bindra Thusu[6], Andrew G. Whitham[1†]

[1] CASP, West Building, Madingley Rise, Madingley Road, Cambridge, CB3 0UD, UK

[2] Abteilung Sedimentologie/Umweltgeologie, Geowissenschaftliches Zentrum Göttingen, Universität Göttingen, Goldschmidtstraße 3, 37077 Göttingen, Germany

[3] Present address: School of Geography, Geology and the Environment, Keele University, Keele, Staffordshire, ST5 5BG, UK

[4] Present address: JBA Consulting, Floor 4, Maybrook House, Grainger Street, Newcastle upon Tyne NE1 5JE, UK

[5] Mellitah Oil & Gas B.V., Dat Al Imad Complex Tower 5 Floor 13, P.O. Box 91651, Tripoli, Libya

[6] Maghreb Petroleum Research Group, Department of Earth Sciences, University College London, Gower Street, London WC1E 6BT, UK

† deceased

* Corresponding author: g.meinhold@keele.ac.uk (G. Meinhold)

Abstract

This paper reports on the elemental geochemistry of 47 shale samples from the uppermost Hirnantian–lowermost Rhuddanian Tanezzuft Formation, collected from drill core (depth interval 20.8–73.2 m) from borehole JA-2 at the eastern Kufra Basin, SE Libya. Eighteen of these samples were also analysed by X-ray diffraction. This study was carried out (i) to search for shales with high total organic carbon (TOC >3 wt%) and associated high uranium (U >30 ppm) concentrations, commonly referred to as 'hot' shales, (ii) to test whether TOC and U correlate, (iii) to study the effects of surface weathering on the behaviour and mobility of major oxides, trace elements and rare earth elements (REE), and (iv) to examine the relationship of the elemental composition obtained in this study and Rock-Eval pyrolysis and kerogen data obtained in previous studies on the same core samples. The studied core can be divided into three intervals: upper weathered section (20.8–46.5 m, influenced by Quaternary weathering), unweathered section (46.5–68.5 m), and lower weathered section (68.5–73.9 m, influenced by latest Ordovician weathering). Overall, the shales have low TOC values (<1 wt %) and low U concentrations (<12 ppm). TOC and U do not show any correlation likely due to their low values. Hence, 'hot' shale has not yet been proven in this part of the Kufra Basin. Trace elements such as Mn and Sc show significant changes from the weathered into the unweathered core section. In contrast, the majority of the major oxides, trace elements and REE seem to be unaffected or at least largely unaffected by weathering processes. The exception is the transition from the unweathered section into the lower weathered section of the core. Here, most of the major oxides, trace elements and REE show either abrupt or gradual shifts towards lower or higher element concentrations. The observed whole-rock geochemical (e.g., K_2O, Rb, Sr, Th/K) and mineralogical (e.g., kaolinite/illite,

K-feldspar/quartz) changes suggest either a switch from one source area to another or, more likely, climatic influence. The deepest part of the core may have been influenced by a more humid and warm climate that has led to intensive chemical weathering and dissolution of K-feldspar. During the latest Hirnantian–earliest Rhuddanian a temporary emersion event may have occurred due to post-glacial rebound, which has led to the weathering of older strata.

Keywords:
Whole-rock geochemistry; X-ray diffraction analysis; Late Ordovician; Early Silurian; Kufra Basin; Libya

1. Introduction

During the Late Ordovician Epoch, large parts of West Gondwana were covered by massive glaciers (e.g., Sutcliffe et al., 2000; Le Heron et al., 2009). Upon melting of the ice sheets in the latest Hirnantian (ca. 444 Ma ago), huge volumes of meltwater and sediment were released and shed to the periphery of Gondwana (e.g., Sutcliffe et al., 2000; Le Heron et al., 2009). In Libya, these sediments are predominantly made up of compositional mature sandstones (Mamuniyat Formation), forming good-quality hydrocarbon reservoirs. Polished and striated surfaces are common features in these sandstones that point to their glaciogenic origin (e.g., Le Heron et al., 2009, 2010, 2015). The Late Ordovician deglaciation was followed by the deposition of black shales in the early Silurian (Tanezzuft Formation), with some of the shales having high total organic carbon (TOC) contents (Lüning et al., 2003; Vecoli et al., 2009; Abohajar et al., 2015; El Diasty et al., 2017a, b, c). These shales are often called ‘hot’ shales because of their associated high uranium (U) concentration. They are the

most important source rock for Early Palaeozoic-sourced hydrocarbons across North Africa (e.g., Lüning et al., 2000). Consequently, both the Upper Ordovician glaciogenic sediments and the lower Silurian 'hot' shales have been the focus of geological investigations in Libya (e.g., Lüning et al., 2000, 2003; Lüning and Fello, 2008; Loydell et al., 2013; Meinhold et al., 2016; El Diasty et al., 2017a, b, c; Stockey et al., 2020).

The Murzuq and Kufra basins are large Palaeozoic basins in southern Libya (Fig. 1). In the Murzuq Basin, a large number of boreholes have been drilled during the last 60 years, seismic data has been acquired, and hydrocarbon reserves are proven. This is in contrast to the Kufra Basin where only a handful of wells have been drilled and a hydrocarbon system is unproven. Fieldwork has confirmed the presence of Late Ordovician glaciogenic sandstones (Mamuniyat Formation) in the Kufra Basin (Fig. 2); equivalent sandstones are a major reservoir for hydrocarbons in the Murzuq Basin. However, the existence of a potential source rock (i.e., lower Silurian 'hot' shales) has not yet been proven in the Kufra Basin.

The Tanezzuft Formation 'hot' shales are seldom exposed and the few outcrops are often strongly weathered. Surface shale samples have commonly lost all organic matter through oxidation and become green and red in colouration (e.g., Lüning and Kolonic, 2003; Lüning et al., 2003; Meinhold et al., 2013a). This makes them unsuitable for source rock and biostratigraphic investigation. Following the retrieval of fresh material from drill core from borehole (CDEG-2a) at the eastern Murzuq Basin (Meinhold et al., 2013a; Paris et al., 2012), using a small portable drilling rig with the ability to obtain a core of about 3 cm in diameter, a borehole more than 70 m deep was drilled through the Tanezzuft Formation at the eastern Kufra Basin in April–May 2009 (Figs. 1 and 3; see Meinhold et al., 2013b for details). In this borehole, unweathered shale was encountered at 46.5 m depth (Fig. 4). The recovered material was used for a Rock-Eval pyrolysis study (Meinhold et al., 2013b) and for

palynological analyses (Thusu et al., 2013). Based on biostratigraphic correlations with chitinozoan-bearing successions straddling the Ordovician–Silurian boundary in Arabia, North Africa and the USA led to the conclusion that the studied samples from borehole JA-2 are post-glacial deposits and are of either latest Hirnantian age, or at least no younger than earliest Rhuddanian (Thusu et al., 2013).

The present study focuses on whole-rock geochemical analysis of drill core material from borehole JA-2. Major oxide, trace element and REE abundances were obtained on 47 shale samples from the Tanezzuft Formation from the 20.80–73.21 m interval. A representative subset of 18 samples was also analysed by X-ray diffraction (XRD) to identify their mineralogy. The upper section of the core from the surface down to about 46.5 m depth displays signs of oxidative weathering (i.e. beige colour of the shale, and oxidation of the organic matter) (for details see Meinhold et al., 2013b). This weathering corresponds likely to the deep sub-Recent weathering profiles found in many places across the Sahara (Thusu et al., 2013). From 46.60 m to 67.82 m depths, the core is unweathered (Fig. 4) as evidenced by its organic matter content (Thusu et al., 2013; Meinhold et al., 2013b). The lithology is relatively constant and ranges from greenish and grey shale to grey siltstone with micas. A lithological change occurs at 67.59–67.82 m depth with the occurrence of very fine sandstone. From 67.97 m to 69.12 m depths, there is a sign of weathering as indicated by the oxidation of pyrite and the brownish colouration of micas, in very fine, light coloured sandstone and the whitish colouration of shale. Moreover, starting at 67.97 m depth, evidence of weathering is indicated by a dramatic decrease in the abundance of chitinozoans (Thusu et al., 2013). The lowermost section between 68.42 m and 73.90 m is weathered and includes a minor fault zone. The palynomorph assemblages recovered from the JA-2 drill core material support a marginal marine depositional environment (Thusu et al., 2013).

The geochemical data of the JA-2 core have been used (i) to study variations in major oxides, trace elements and REE as amounts of weathering increase, (ii) to study the relationship between other elements and Rock-Eval analysis data, and compare with data obtained in a previous study by Meinhold et al. (2013a), and (iii) to study the relationship between TOC and uranium (U) content. The latter is of special importance because U values between 10 and 30 ppm are considered to be typical for 'warm' shales while values >30 ppm are commonly considered to represent 'hot' shales, meaning shales with TOC content >3 wt% (e.g., Lüning et al., 2000, 2003; Lüning and Fello, 2008).

Portable gamma-ray spectrometry (PGRS) is widely used to measure the U content of the Tanezzuft Formation shales at outcrop to search for 'warm' shales and 'hot' shales in southern Libya (e.g., Lüning et al., 2003; Lüning and Fello, 2008; Meinhold et al., 2016). However, a whole-rock geochemical study on core material from the Tanezzuft Formation in Dor el Gussa (Meinhold et al., 2013a) has shown that TOC contents do not correlate with U abundances, at least in the range of low TOC. Therefore, total U contents obtained with PGRS on outcrop samples may not always reflect the true TOC content in the rock. Samples between 0.5 and 1.5 wt% TOC can still have moderate–good source potential of >3.5 kg/tonne, and are not associated with high U values (Meinhold et al., 2013a). Hence, absence of high U values is not necessarily evidence of a lack of source potential, only of reduced source potential (Meinhold et al., 2013a). The present study will provide further insight on this subject and the applicability of PGRS for 'hot' shales search in southern Libya and in other deeply weathered sections.

2. Analytical techniques

2.1. ICP-MS analysis

The drill core material was disintegrated into small pieces with a hammer and then powdered using an agate ball mill. Finely ground rock powder was dissolved by acid digestion with HF–HNO_3 using an Evapoclean® system and later analysed using a PerkinElmer SCIEX Elan DRC II inductively coupled plasma–mass spectrometer (ICP–MS) at the Department of Earth Sciences, University of Cambridge, following the methodology as outlined in Meinhold et al. (2013b). International rock standards were measured as unknown in this study for quality control. Values for the BCR-2 and BHVO-2 standards measured in this study and reported values from the literature for comparison are given in Supplementary Table S1 and Table S2, respectively, in Appendix A.

2.2. XRD analysis

To obtain information about the mineralogical composition of drill core from borehole JA-2, X-ray diffraction (XRD) analysis was carried out on 18 representative samples. Randomly oriented powder samples were analysed with a Panalytical X'Pert Pro diffractometer at the School of Ocean and Earth Science, University of Southampton, following the methodology as outlined in Meinhold et al. (2016).

3. Results

3.1. Whole-rock geochemistry

169 Geochemical results of 47 shale samples (20.80–73.21 m depth) are presented in
170 Supplementary Table S3 (see Appendix A). Major oxides, trace elements and rare earth
171 elements (REE) obtained in this study, calculated key parameters (e.g. $U_{authigenic}$, Ce-anomaly)
172 and in addition TOC and hydrogen index (HI) (data from Meinhold et al., 2013b) have been
173 plotted against depth in Figures 4 to 8. Selected elements and element ratios are additionally
174 shown on cross plots in Figures 9 to 13. Following common practise, the REE data are shown
175 on both chondrite- and post-Archaean Australian Shale (PAAS)-normalised diagrams (Fig.
176 14). Normalisation values for chondrite (CI) and PAAS were taken from Taylor and
177 McLennan (1985) and McLennan (1989), respectively.
178
179 *3.1.1. Element relationships with depth*
180
181 In general, most elements show a homogenous distribution in the weathered section between
182 depths of 20.80 m and about 46.50 m (except one sample at the depth of 27.27 m) and in the
183 unweathered section between depths of about 46.50 m and 68.50 m. However, the lowermost
184 part of the unweathered section and the section below (starting at a depth of about 65 m down
185 to the final depth of 73.90 m) show for most of the elements a significant increase or decrease
186 in element concentrations respectively.
187 Throughout the core, the actinide metal uranium (U) has element concentrations
188 between 3.1 and 5.3 ppm (mean value ~ 4.1 ppm); the exception is the lower part of the core
189 at the depth of about 67.82 m towards the base of the core where U concentrations are
190 between 6.8 and 11.9 ppm (mean value ~ 8.7 ppm) (Fig. 5). These values are above the
191 average for PAAS of 3.1 ppm (Taylor and McLennan, 1985).

Thorium (Th) concentrations range between 11.0 and 48.6 ppm (Fig. 5), with a mean value of 17.7 ppm. This includes three samples with significant higher values (22.8 ppm at the depth 27.27 m, 26.6 ppm at the depth of 67.82 m and 48.6 ppm at the depth of 68.42 m) and two samples with significant lower values (11.0 ppm at the depth of 62.34 m and 11.6 ppm at the depth of 64.55 m) than the mean value of 17.7 ppm.

Throughout the core down to the depth of 67.59 m the Th/U ratios are quite constant with 3.6 to 4.8, whereas starting at the depth of 67.82 m towards the base of the core the Th/U ratios are 1.7 to 2.2 and thus significantly lower than in the section above (Fig. 5). The exception is the sample at 68.42 m depth, which has a Th/U ratio of 4.4. Note that this sample has the highest Th content of all samples (48.57 ppm).

Authigenic (non-detrital) U content (Wignall and Myers, 1988), calculated as

$$U_{authigenic} = (\text{total U}) - Th/3,$$

and Th/U ratios show similar but inverse patterns. Positive values for $U_{authigenic}$ (1.97 to 4.06 ppm) are only observed in the lower section of the core, at the depth of 67.82 m toward to the base of the core (Fig. 5).

An interesting parameter is cerium (Ce), which is commonly examined as Ce-anomaly. Ce-anomaly values are commonly used in marine deposits for reconstructing palaeo-redox conditions and sea-level changes (e.g. Murray et al., 1990; Wilde et al, 1996; Pattan et al., 2005, and references therein). This is because Ce is sensitive to changes in the redox state of the ocean but lanthanum (La) and promethium (Pr) are not. In the present study, the Ce-anomaly values were calculated according to Murray et al. (1990):

Ce-anomaly = Ce/Ce* = $Ce_{SN}/(0.5La_{SN} + 0.5Pr_{SN})$,

where SN indicates normalization to post-Archaean Australian Shale (PAAS; Nance and Taylor, 1976), with values taken from McLennan (1989). Values of Ce/Ce*>1 are considered to be positive, whereas values <1 are considered to be negative. The whole-rock Ce-anomaly values of the studied samples fluctuate around 0.93 (±0.06), with exceptions of 0.78 and 1.08 at the depths of 55.53 m and 73.20 m respectively (Fig. 5).

Potassium (K), expressed as K_2O, varies between 2.94 and 3.67 wt%, with a mean value of 3.37 wt%, at depths between 20.80 m and 64.02 m (Fig. 5). The section below, between 64.55 and 73.21 m, has K_2O contents between 1.48 and 2.68 wt%, with decreasing values toward the base of the core.

Th/K ratios vary around 5 for most samples down to a depth of 64.55 m, whereas samples at the depth of 65.23 m and below show higher Th/K ratios of up to ~18 (Fig. 5). Rubidium (Rb) and K_2O contents show similar patterns (Fig. 5). Rb values vary between 117 and 167 ppm, with a mean value of 140 ppm, at depths between 20.80 m and 63.45 m, whereas samples at the depth of 64.02 m and below show (after a transitional interval) lower K_2O contents, with values decreasing toward ~60 ppm at the depth of 73.21 m (Fig. 5). Interestingly, strontium (Sr) and Rb contents show similar but inverse patterns (Fig. 5). Sr values vary between 66 and 100 ppm, with a mean value of 83 ppm, at depths between 20.80 m and 63.45 m, whereas samples at the depth of 64.02 m and below show (after a transitional interval) higher Sr contents, with values increasing toward ~188 ppm at the depth of 73.21 m (Fig. 5). Note that Rb/Sr ratios and K_2O contents show similar patterns.

Phosphorous (P), expressed as P_2O_5, shows little variation and has concentrations between 0.07 and 0.20 wt%, with few samples having slightly higher values (Fig. 5;

240 Supplementary Table S3). Note that two samples from the uppermost section of the core at
241 the depths of 20.80 m and 27.27 m have significantly higher P_2O_5 values of 0.34 and 0.59 wt
242 % respectively.

243 Titanium (Ti), expressed as TiO_2, and niobium (Nb) show similar trends (Figs 5, 6).
244 TiO_2 and Nb contents vary between 0.95 and 1.29 wt% and between 19 and 25 ppm
245 respectively. Both elements show their highest values at the depths of 27.27 m (1.23 ppm
246 TiO_2, 24 ppm Nb) and 67.82 m (1.29 wt% TiO_2, 25 ppm Nb).

247 Scandium (Sc) shows a distinctive pattern (Fig. 6). In the weathered section, Sc values
248 range from 16 to 27 ppm (mean value ~ 23 ppm), while in the unweathered section they are
249 mainly lower and range between 11 and 30 ppm (mean value ~ 15 ppm). The lowermost
250 section between depths of 68.42 m and 73.21 m has again higher Sc values (25–31 ppm; mean
251 value ~ 28 ppm), which are even higher than those of the weathered section between 20.80 m
252 and 46.20 m depths.

253 Vanadium (V) shows little variance between the weathered and unweathered sections
254 (Fig. 6). Most of the samples have V values between 110 and 150 ppm (mean value ~ 130
255 ppm). The two highest values of 164 and 160 ppm occur at depths of 71.44 and 72.07 m,
256 respectively. Note that the sample at the depth of 27.27 m has also an elevated V content (150
257 ppm).

258 Chromium (Cr) shows little variance between the weathered and unweathered sections
259 (Fig. 6). Concentrations vary between 70 and 110 ppm, with a mean of 90 ppm. Values less
260 than 70 ppm are observed at depths of 43.84 m (66 ppm), 62.34 m (60 ppm) and 64.55 m (63
261 ppm), and values higher than 110 ppm occur at depths of 27.27 m (111 ppm), 67.05 m (114
262 ppm), 67.97 m (111 ppm) and 68.42 m (111 ppm).

Manganese (Mn) concentrations allow a clear subdivision of the core into three sections, which seems to coincide with the subdivision based on the grade of weathering (Fig. 6). In the weathered section, between 20.80 and 46.20 m, Mn concentrations vary from 258 to 648 ppm (mean value ~ 413 ppm). Concentrations in the unweathered section are between 494 and 2412 ppm (mean value ~ 1290 ppm). The exceptions are single values of 6048 ppm and 4042 ppm at depths of 64.55 m and 67.40 m, respectively, as well as values of 374, 388 and 179 ppm at depths of 46.60 m, 67.59 m and 67.82 m, respectively, which are the uppermost and the two lowermost samples of the unweathered section. Samples from the lowermost section of the core show Mn concentrations less than 160 ppm.

Copper (Cu) concentrations mainly vary between 30 and 51 ppm (mean value ~ 43 ppm), the exception is a single peak of 64 ppm at 61.51 m depth and values of less than 30 ppm in the deepest part of the core between 68.42 and 73.21 m depth (Fig. 6).

With the exception of a few single peaks, zinc (Zn) and cobalt (Co) show similar patterns with an increase in element concentrations with increasing depth, which is especially apparent in the lower part of the unweathered section (Fig. 6). However, the deepest part of the unweathered section, starting at 67.82 m records an abrupt decline of Co and Zn concentrations to values of less than 10 and 50 ppm respectively. Such low values characterise the 67.82 to 73.12 m interval.

Element concentrations of nickel (Ni) are around 50 ppm and do not show much variation within most of the core to a depth of 62.34 m (Fig. 6). The 62.75 to 67.59 m interval records elevated Ni contents of up to 86 ppm and even two single peaks with values of 162 and 157 ppm (at 64.02 m and 67.59 m respectively) are present. The remaining 67.82 to 73.12 m interval shows a subsequent decrease in Ni concentration from 50 to 10 ppm.

Element concentrations of the light element lithium (Li) vary between 71 and 129 ppm (mean value ~ 110 ppm), the exception is a single peak at the depth of 57.59 m (182 ppm of Li) and values of less than 70 ppm in the lowermost part of the core between 68.42 m and 73.21 m depth (Fig. 6).

The light element beryllium (Be) shows an interesting pattern. Its concentrations are between 2.2 and 3.8 ppm throughout the core between 20.80 and 64.55 m depth. Higher values than 3.8 ppm (up to 7.6 ppm) are recorded between 65.23 and 69.12 m depth, and the lowermost part of the core is again characterised by low Be concentrations of about 2.3 to 2.7 ppm (Fig. 6). Interestingly, Li/Be ratios mainly fluctuate between 30 and 40 ppm at depths between 20.80 m and 65.74 m, the exception is a sample at the depth of 43.84 m with a Li/Be ratio of about 21 (Fig. 6). Samples between 66.21 m and 73.21 m have Li/Be ratios of less than 30 with the Li/Be ratios showing a continues decrease down to values of about 20 ppm.

Element concentrations of tin (Sn) vary between 3 and 5 ppm (mean value ~ 4.2 ppm). The exception is the sample at 67.05 m depth with about 6 ppm of Sn (Fig. 6). Moreover, from 20.80 m to 73.21 m depths there seems to be a trend towards higher Sn values with increasing depth.

Throughout the core, yttrium (Y) concentrations mainly vary between 20 and 40 ppm (mean value ~ 29 ppm), the exceptions are few samples with higher values (see Fig. 7).

Zirconium (Zr) concentrations are mainly ranging between 90 to 140 ppm (mean value ~ 113 ppm); the exception is a single sample at the depth of 65.23 m with 189 ppm of Zr (Fig. 7).

Throughout the core, element concentrations of the alkali metal caesium (Cs) mainly vary between 6 and 8 ppm (mean value ~ 7 ppm), the exceptions are few samples with higher and lower values respectively (Fig. 7).

Barium (Ba) shows an interesting pattern (Fig. 7). After a slightly fluctuating pattern with Ba concentrations between 618 and 720 ppm in the weathered section and the uppermost part of the unweathered section between 20.80 and 62.75 m depth, the Ba concentration decreases between 63.14 m and 67.97 m depth to a value of about 460 ppm, followed by an increase in Ba concentrations (values up to 811 ppm) in the deepest section of the core after a single spike of 1403 ppm of Ba at the depth of 68.42 m.

Throughout the core, hafnium (Hf) concentrations are between 3 and 4 ppm (mean value ~ 3.4 ppm), the exceptions are samples at the depths of 62.34 m, 64.55 m, 65.23 m and 67.40 m with Hf concentrations of about 2.8, 2.9, 5.0 and 2.7 ppm respectively (Fig. 7). For almost all samples, the Zr/Hf ratios range between 32 and 35, with a mean value of ~ 34 (not shown on any diagram).

Element concentrations of tantalum (Ta) do not show any obvious pattern. The Ta values fluctuate around 1.5 ppm, with only two single peaks at 27.27 m and 67.82 m depth showing significantly higher values of up to almost 1.8 ppm of Ta (Fig. 7).

Throughout the core, total concentrations of the rare earth elements (REE) vary between 200 and 310 ppm (mean value ~ 246 ppm), with exceptions at depths of 27.27 m, 67.82 m and 68.42 m where the total REE concentrations are 534, 394 and 825 ppm respectively (Fig. 7).

As expected, the REEs from lanthanum (La) to lutetium (Lu) show similar patterns and do not show much variation for each element (Fig. 8). The exceptions are two samples from the uppermost section of the core, at 20.80 m and 27.27 m depths, and two samples from the lower section of the core, at 67.59 m and 68.42 m depths, which have significantly higher values for most of the REEs. Regarding the last two samples, following observation can be made. At 67.59 m depth, there is an increase towards higher values from lanthanum (La) to

lutetium (Lu) whereas at 68.42 m depth the REEs behave exactly opposite with decreasing values from lanthanum (La) to lutetium (Lu). Note that of all analysed samples the sample at 67.59 m depth has also the highest concentration of yttrium (155 ppm) (Fig. 7).

3.1.2. Binary plots

TOC and HI do not correlate with U (Fig. 9). The highest TOC content of 0.75 wt% has a U content of 4.7 ppm, whereas the highest U content of 11.9 ppm shows only a TOC content of 0.46 wt%. Note that the highest U content belongs to a sample from the deepest part of the unweathered core section. It therefore cannot be excluded that the TOC content of 0.46 wt% has already been slightly influenced by weathering and hence may already be an artifact. Originally, the TOC content of this U-rich sample might have been higher. Uranium also shows no correlation with Zr concentrations (Fig. 10a). Hafnium (Hf) however correlates positively with Zr, where $R^2 = 0.94$ (Fig. 10b). Rubidium (Rb) correlated positively with K_2O, where $R^2 = 0.90$ (Fig. 11a), but negatively with strontium (Sr), where $R^2 = 0.61$ (Fig. 11b). It is worth noting that samples with high U concentrations (>6 ppm) have Rb/Sr ratios of less than ~ 1 (Fig. 12a). Furthermore, most of the samples with high U concentrations have Th/K ratios greater than 9 (Fig. 12b).

Niobium (Nb) correlates positively with TiO_2, where $R^2 = 0.96$ (Fig. 13a), and nickel (Ni) correlates positively with cobalt (Co), where $R^2 = 0.90$ (Fig. 13b). However, for the latter calculation, samples with Ni/Co ratios of about 4 and greater were excluded (i.e., the sample at 64.02 m depth and samples from 67.59 to 69.12 m depths).

3.1.3. Normalised REE diagrams

Shale samples from borehole JA-2 (Fig. 14) show similar REE patterns, regardless of depth, however, REE abundances are higher in samples at depths of 20.80 m, 27.27 m and 68.42 m (Fig. 14a,b,m,n). One exception is the sample at 67.59 m depth, which shows a distinct REE pattern. All samples show chondrite-normalised patterns with light REE enrichment and flat heavy REE patterns with negative europium (Eu) anomalies. PAAS-normalised REE concentrations show almost flat patterns with light REE enrichment. The sample from 67.59 m depth shows similar chondrite- and PAAS-normalised patterns for the light REE but significant enrichment in the middle and heavy REE (Fig. 14m,n).

3.2. XRD analysis

XRD analysis revealed that quartz, K-feldspar, kaolinite and illite form the prominent mineral assemblage (Fig. 15; Supplementary Table S4). Chlorite, siderite and pyrite are also present in many samples but only in minor amounts. With the exception of two samples, quartz, K-feldspar, kaolinite and illite show constant values with only minor fluctuations throughout most of the core from 20.80 m to about 65 m depths, whereas from 65 m towards the base of the core either a significant increase or decrease of these minerals is recorded. The kaolinite/illite ratio fluctuates around 1 from 20.80 m to about 65 m depths, whereas the deeper section of the core shows a constant increase of the kaolinite/illite values to up to almost 4 (Fig. 15). The K-feldspar/quartz ratios are between 0.2 and 0.5 from 20.80 m to about 65 m depths, whereas the deeper section of the core records a constant decrease in the K-feldspar/quartz ratio (Fig. 15). The K-feldspar content correlates negatively with Th/K and positively with K_2O (Fig. 16). The K-feldspar content also correlates negatively with Rb (Fig.

17a), whereas the illite content correlates positively with the Rb content, where $R^2 = 0.83$ (Fig. 17b). The K-feldspar/illite ratios correlate positively with the Sr content (Fig. 18a) and show a negative correlation with the K-feldspar/quartz ratios (Fig. 18b).

4. Discussion

4.1. Whole-rock geochemistry

4.1.1. Element relationships with depth

Core from JA-2 in Jebel Asba can be subdivided into three sections based on the grade of weathering, which is expressed by colour changes from orange/brown (upper weathered section) to dark grey (unweathered section) and further to light grey/reddish (lower weathered section) (Fig. 4). Trace elements such as Mn and Sc show changes from the weathered into the unweathered section whereas the majority of the major oxides, trace elements and REE seem to be unaffected, or at least little affected, by weathering processes. The exception is the transition from the unweathered section into the lower weathered section. Here, most of the major oxides, trace elements and REE show either an abrupt or gradual shift towards lower or higher element concentrations.

In the upper weathered section and in the unweathered section down to 67.59 m depth, the U contents are about 4.1 ppm, which can be seen as normal (background) value of U for the Tanezzuft Formation shales in Jebel Asba. The elevated U concentrations (6.8–11.9 ppm) found in the deepest part of the core (67.82–73.21 m depth) are not related to heavy mineral (zircon) enrichment. Here, the U enrichment is of authigenic origin as suggested by positive

406 values for $U_{authigenic}$ (1.97 to 4.06 ppm). U enrichment in sediment is commonly seen as an
407 indication of reduced oxygen levels in bottom waters and increased amounts of organic matter
408 (McManus et al., 2005). This is a possible explanation for the observed U enrichment in the
409 deepest section of the JA-2 core.

410 With Th concentrations being fairly constant throughout the core and U concentrations
411 showing a significant increase in the lower part of the core (Fig. 5), the Th/U ratios allow a
412 clear subdivision of the core into two sections. Throughout the core down to 67.59 m depth
413 the Th/U ratios are quite constant with 3.6 to 4.8, whereas starting at the depth of 67.82 m
414 towards the base of the core the Th/U ratios are 1.7 to 2.2; here they are significantly lower
415 than in the section above (Fig. 5). The exception is the sample at 68.42 m depth with Th/U of
416 4.4.

417 Before an explanation is given for these different Th/U ratios, the following outline
418 will help in understanding of the behaviour and mobility of U and Th in the sedimentary
419 environment. Geochemically, U and Th behave similarly, except under oxidising conditions
420 (McLennan et al., 1993, and references therein). Thorium is relatively immobile and is present
421 chiefly in the detrital clay minerals (e.g., Pattan et al., 2005, and references therein). It is not
422 affected by redox conditions and is present as insoluble Th^{4+} in the marine environment.
423 Uranium, however, is mobile under oxidising conditions as soluble U^{6+}. Under strongly
424 reducing conditions, U^{6+} may be reduced to the immobile U^{4+}, leading to U enrichment in
425 sediments, while oxidising environments can cause U loss from sediments (Klinkhammer and
426 Palmer, 1991; Jones and Manning, 1994; Wignall and Twitchett, 1996). Average shale such
427 as PAAS is an integrated average of the composition of the upper continental crust and has a
428 Th/U ratio of 3.8 (Taylor and McLennan, 1985). Under normal oxidising conditions, marine
429 shale commonly retains this ratio or higher because the soluble form of U will be favoured

(Guo et al., 2007). Yet, some U may be sequestered during early diagenesis due to reducing conditions in pore waters related to organic decomposition (Guo et al., 2007). Wignall and Twitchett (1996) have suggested that depositional environments with anoxic conditions lead to shale Th/U ratios of 0 to 2, and this has been commonly used as a guideline in subsequent studies. For example, Kimura and Watanabe (2001) showed that only sediment with Th/U ratios <2 exhibited no recognizable bioturbation in their study of the lower Cambrian shales from Iran, thus providing firm evidence that Th/U of ~2 seems to be an appropriate cut-off point in distinguishing anoxic from oxic bottom waters.

Returning to the JA-2 core sample, shales from 20.80 m to 67.59 m depths exhibit fairly constant Th/U ratios of 3.6 to 4.8, whereas the deeper section of the core has Th/U ratios of 1.7 to 2.2, with one exception of 4.4 at 68.4 m depth. Thus, most parts of the core between 67.82 and 73.21 m depths has Th/U ratios in the range of the proposed cut-off point between anoxic and oxic bottom waters (Wignall and Twitchett, 1996). This would suggest an anoxic environment during the period of deposition recorded in this cored interval. The presence of authigenic U seems to confirm this statement, as sediment enriched in authigenic U tends to have been deposited under highly reducing conditions that allow a large amount of organic matter to accumulate to which U is fixed (Wignall and Myers, 1988). However, Wignall and Myers (1988) also noted that carbonate and phosphate minerals could incorporate U, which would limit the application of authigenic U content to identify anoxic environments in the sedimentary record. This is likely the case for the core sample from 68.42 m depth, which has a U content of 11 ppm accompanied by a P_2O_5 content of 0.77 wt% (Fig. 5). The latter is about 7 times higher than the average P_2O_5 content observed in the JA-2 core.

Ce anomalies of the studied samples are around 0.93 (±0.06), with exceptions of 0.78 and 1.08 at the depths of 55.53 m and 73.20 m respectively (Fig. 5). Thus, with the exception

454 of these two samples, the shales of the JA-2 core were likely deposited during fairly stable
455 palaeo-ocean water redox conditions. It is pertinent here to discuss briefly the behaviour of Ce
456 in ocean water. Ce^{3+} acts like other REE but oxidised Ce^{4+} is less soluble and is easily
457 adsorbed by any Mn-, Fe-oxyhydroxide (Möller et al., 1994) or organic particles (Holser,
458 1997). This consequently results in Ce depletion with negative anomalies in seawater and
459 positive or less negative anomalies in the sediment. In an anoxic environment, Ce is mobilised
460 and released into seawater as Ce^{3+}, causing its positive anomalies in seawater and depletion
461 with negative anomalies in contemporaneous sediments (De Baar et al., 1985; Wilde et al.,
462 1996). Note that some organisms remove phosphate from seawater and thus inherit the REE
463 pattern of seawater. Their Ce anomaly will be opposite in the form to that of coeval sediment.
464 It is however worth noting that any primary signature may be overprinted by late diagenetic
465 modification (MacLeod and Irving, 1996; Holser, 1997). The use of the whole-rock Ce
466 anomaly of sediment to reconstruct palaeo-ocean redox conditions needs to be applied with
467 caution (Patton et al., 2005) if no other parameters are available.
468 Significant changes throughout the core are exhibited by K_2O, Th/K, Rb, Sr and
469 Rb/Sr, with either increasing or decreasing values towards the base of the core (Fig. 5). A
470 decrease in K_2O content accompanied by increasing Th/K values toward the base of the core
471 suggests a decrease in K-feldspar content. This may reflect a change in the source area or of
472 climate; a more humid warm climate would have led to intensive weathering and dissolution
473 of K-feldspar in the source area.
474 The change in Rb, Sr and Rb/Sr values with depth seems to confirm a change in
475 palaeo-climate conditions. Due to their different geochemical behaviour, Rb and Sr are easily
476 fractionated during common processes at the Earth's surface such as weathering (e.g., Jin et
477 al., 2001, 2006). Because of that, changes of Rb/Sr ratios have been used as proxy for

chemical weathering intensity. Weathering profiles often show a negative relationship between the Sr concentration and the Rb/Sr ratio due to an affinity of Rb for clay minerals and Sr loss to solution during weathering (e.g., Jin et al., 2001, 2006). Studies on weathering profiles and loess–palaeosol successions provide evidence that the Rb/Sr ratios in weathering products increase notably with the enhancement of weathering intensity (e.g., Jin et al., 2001, 2006). Consequently, intensification of weathering increases the supply of Sr into the basin, resulting in lower Rb/Sr ratios in lake and marine sediments (e.g., Jin et al., 2001, 2006). Transferring this to the JA-2 core, the constant increase in Rb/Sr values from the base toward the top of the core suggests that the source area providing the sediment that forms the lower part of the JA-2 core between 73.21 and about 67 m experienced an enhancement of weathering intensity compared to the core above.

The elevated value of phosphorous for the sample at 27.27 m depth (Fig. 5) is likely related to the occurrence of a phosphatic phase, which could reflect either detrital input from the continent (e.g., detrital apatite) or a biogenic origin. Since this sample has also elevated Ti, Th, Rb, Y and REE values (Figs 5, 7 and 8; Supplementary Table S3), a major detrital influx from the continent is most likely.

The Sc content shows significant changes throughout the core (Fig. 6), with ~23 ppm between 20.80 and 46.20 m depth, ~15 ppm between 46.60 and 67.21 m depth, and ~28 ppm between 67.40 and 73.21 m depth. The Sc values in the latter section are even higher than those of the weathered section between 20.80 m and 46.20 m depths. Before an explanation is given for these different Sc values, the following outline will help understanding of the geochemical behaviour of Sc. Because the radius of Sc^{3+} (0.81 Å) is close to that of Fe^{2+} (0.74 Å), and the electronegativity of Sc^{3+} (E_{Sc} = 1.3) is much smaller than that of Fe^{2+} (E_{Fe} = 1.65), Sc exhibits a great tendency to enter a suitable crystal lattice to replace Fe^{2+} during magmatic

crystallisation (Ringwood, 1955). Although the behaviour of Sc is complex, there seems to be a close geochemical coherence between Sc^{3+} and Fe^{2+} (plus Fe^{3+}). Moreover, Sc^{3+} can substitute for Al^{3+} and Ti^{3+}. Scandium is mainly associated with ferromagnesian minerals and biotite, and it can be enriched in phosphorites (Kabata-Pendias and Mukherjee, 2007). Judging from these evidences, it is suggested that Sc enrichment in the lower and upper sections of the JA-2 core may simply be related to Fe enrichment due to intense chemical weathering. Note that Sc is commonly taken as a reliable indicator of terrigenous material, mainly aluminosilicates, which may provide an alternative explanation for the observed Sc values in the JA-2 core. Unfortunately, an extensive discussion here concerning the behaviour of Sc in fine-grained clastic sediment is hampered by the lack of published literature.

Elements such as Mn, Co and Zn show low values in the weathered section between 67.82 and 73.21 m depths, compared to the section between 20.80 and 67.59 m depths. The element concentrations are even lower than those of the upper continental crust (Mn ~ 600 ppm, Co ~ 10 ppm, Zn ~ 71 ppm; Taylor and McLennan, 1985). The depletion in the lower weathered section may simply be a result of element leaching due to intensive chemical weathering.

Interestingly, high Ni/Co ratios occur in the lower part of the JA-2 core. Ni/Co ratios are 4.1 to 8.6 between 67.59 and 69.12 m depths and 2.8 to 3.5 between 71.44 and 73.21 m depths, compared to only about 2.2 in the section between 20.80 and 67.40 m depths. Ni is controlled by the sulphide content since Ni resides in framboidal pyrite and covaries with sulphur (Jones and Manning, 1994). Jones and Manning (1994) used Ni/Co to identify the oxygen status during shale deposition. They concluded that shale deposited under oxic conditions (860–2.0 ml l^{-1} oxygen) would usually have Ni/Co ratios <5, shale deposited under dysoxic conditions (2.0–0.2 ml l-1 oxygen) would have Ni/Co ratios between 5 and 7 whereas

526 anoxic conditions lead to Ni/Co ratios of ≥7. Therefore, the presence of high Ni/Co ratios in
527 shales of the lower part of the JA-2 core would suggest dysoxic to anoxic conditions during
528 their deposition. However, judging from the extraordinary low Co values it is more likely that
529 the Ni/Co ratios of the lower part are modified by element mobilisation due to intensive
530 chemical weathering.

531 The element concentrations of Y and Zr are fairly constant throughout the core with a
532 few single peaks occurring. The high Y value of 155 ppm at 67.59 m depth is accompanied by
533 elevated HREE concentrations and thus suggests garnet enrichment in this sample. The high
534 Zr value of 189 ppm at 65.23 m depth is probably caused by zircon enrichment. Nearly
535 constant Zr/Hf ratios (32 to 35) throughout the JA-2 core suggest that zircon is the main
536 contributor for Zr and Hf in the analysed sediment.

537 Ba concentrations decrease from high values of about 810 ppm in the lowermost
538 section of the core to values of about 443 ppm at 67.40 m depth, followed by an increase in
539 Ba concentration to values of about 700 ppm towards the top of the core (Fig. 7). The
540 exception is a value of 1403 ppm Ba at 68.42 m depth. In marine sediments, breakdown of
541 organic matter releases Ba into the water column, which in the presence of sulphate forms
542 barite ($BaSO_4$). Thus, Ba is mainly a residue of biogenic material and is therefore often taken
543 as a palaeo-productivity indicator (e.g., Dymond et al., 1992; McManus et al., 1998, and
544 references therein). However, diagenetic redistribution of Ba limits its use as a palaeo-
545 productivity indicator in nearshore deposits, and therefore, Ba from such sediments should not
546 be used for palaeo-productivity reconstructions (Dymond et al., 1992). For example, a
547 diagenetic Ba front can form at the base of the sulphate zone (Dymond et al., 1992, and
548 references therein).

549 Returning to the JA-2 core, the high value of Ba (1403 ppm) at 68.42 m depth is
550 accompanied by high values of P_2O_5 (0.77 wt%), U (11 ppm) and total REE (825 ppm). This
551 suggests a detrital origin for Ba, probably associated with a U–REE-bearing phosphate. The
552 high Ba values in the lowermost section of the core may be explained either by sedimentary
553 influx of Ba-rich detrital material or by post-depositional redistribution of Ba due to intensive
554 chemical weathering. The constant increase of the Ba content in the unweathered section
555 toward the top may reflect an increase in palaeo-productivity. However, Ba does not correlate
556 with the TOC content, and therefore, Ba cannot be used as a palaeo-productivity indicator in
557 the JA-2 core.
558 High total concentrations of the REE of 534 ppm and 825 ppm at 27.27 m and 68.42
559 m depths, respectively, are accompanied by high P_2O_5 values of 0.59 wt% and 0.77 wt%,
560 respectively (Figs 5 and 7). This suggests that detrital phosphate is likely enriched at these
561 depths causing positive peaks for total REE and P_2O_5 concentrations.
562
563 *4.1.2. Binary plots*
564
565 TOC and HI do not correlate with U (Fig. 9). Therefore, other U-bearing phases than those of
566 organic matter must be present, which significantly control the total U content of sediment.
567 The prime candidate is the heavy mineral zircon, which can incorporate significant amounts
568 of U (300–3000 ppm of U; Bateman, 1985). Zircon yields a background value for U in the
569 sediment. The positive correlation between Hf and Zr (Fig. 10b) clearly suggests zircon is the
570 major Hf source in the sediment.
571 The positive correlation between Rb and K_2O (Fig. 11a) suggests that Rb is fixed in K-
572 feldspar since K_2O correlates positively with the K-feldspar content determined by XRD (Fig

16b). Although Rb correlates positively with the K-feldspar content (Fig. 17a), Rb shows a much better positive correlation with the illite content (Fig. 17b). Therefore, illite and minor K-feldspar is likely the carrier of Rb in the JA-2 sediments. The negative correlation between Rb and Sr (Fig. 11b) reflects the different behaviour of Rb and Sr during chemical weathering (see Section 3.1.1. for discussion). Note that high Sr and low Rb contents (plus Rb/Sr < 1) in the highly weathered section (Th/K > 9), in the deepest part of the JA-2 core are accompanied by high kaolinite contents (>35 %) and high kaolinite/illite ratios (>1.5). Therefore, elevated U concentrations (>6 ppm) of samples from this part of the core are likely related to intense chemical weathering. The significant change in whole-rock geochemical composition and mineralogy in the lower part of the JA-2 core is also reflected in a dramatic drop of the abundance of the chitinozoans (Thusu et al., 2013), potentially related to the oxidation noticed on the core samples. Two possible explanations are as follows: (a) a temporary emersion event may have occurred during the lastest Hirnantian–earliest Rhuddanian post-glacial rebound, which led to the weathering of older strata. Interestingly, a hiatus has been predicted to occur between the Hirnantian shale and the Tanezzuft 'hot' shales in core of the Murzuq Basin (unpubl. data, Repsol Oil Operations, Tripoli, cited by Fello et al., 2006, p. 109). (b) Groundwater circulation in a minor fault as observed in the lower part of the core is likely to generate the oxidation of the sediment and of its organic matter in the deeper part of the core.

The positive correlation between Nb and TiO_2 (Fig. 13a) is due to the presence of detrital rutile as it is the most prominent TiO_2 polymorph and a major carrier of Nb and Ti (e.g., Meinhold, 2010). The positive correlation between Ni and Co (Fig. 13b) is due to their similar chemical properties, allowing them to substitute each other in various phases.

4.1.3. Normalised REE diagrams

REEs are widely used to study marine sediments as they are an extremely coherent group of elements (e.g., Elderfield and Greaves, 1982; McLennan, 1989; McLennan et al., 1993). The REEs exist predominantly in the trivalent oxidation state, and their chemical properties vary gradually along the series from lanthanum (La) to lutetium (Lu). Cerium (Ce) and europium (Eu) are exceptions because Ce can be oxidised to a tetravalent state (Ce^{4+}) and then occurs as a solid phase (CeO_2) that is highly insoluble in seawater (Elderfield, 1988). Reduction of Eu to a divalent state (Eu^{2+}) may also occur (De Baar et al., 1983; Elderfield, 1988). Here, we refer to Elderfield (1988), McLennan (1989) and McLennan et al. (1993) for details about the geochemical behaviour and mobility of REEs and their use in sediment geochemistry.

Normalised REE concentrations in shale samples from the shallow borehole JA-2 (Fig. 14) show similar patterns suggesting no significant change in the source area through time. The exceptions are two samples at 67.59 m and 68.42 m depths respectively. The sample from 68.42 m depth has a similar REE pattern as the others samples but all REEs are enriched resulting in a higher total REE whole-rock content (Fig. 14m,n). This can be explained by REE scavenge in a phosphate phase since this sample has the highest phosphate content of all analysed samples. The sample from 67.59 m depth has a similar LREE pattern as the other samples but significant higher concentrations of HREE (Fig. 14m,n). This can be explained by detrital enrichment in garnet since this sample has also a high whole-rock yttrium content.

4.2. XRD analysis

620 Only minor fluctuating values for the quartz, K-feldspar, kaolinite and illite contents
621 throughout most of the core from 20.80 m to about 65 m depth suggest that sediment from
622 this part of the core was most likely sourced by the same hinterland, which did not experience
623 significant changes in climatic conditions. Post-depositional weathering on the whole-rock
624 mineralogy had only minor or no influence. However, the sediment between 65 m and the
625 base of the core shows a significant drop in illite and K-feldspar contents accompanied by an
626 increase in the contents of kaolinite and quartz. Hence, the kaolinite/illite and
627 K-feldspar/quartz ratios show increasing and decreasing values respectively. The deeper part
628 of the JA-2 core therefore records enhanced palaeo-weathering in the sediment source area
629 (see Section 3.1.2. for discussion).
630
631 *4.3. Note on U content in sediment as TOC indicator*
632
633 An important element of our work on the Tanezzuft Formation is to test the relationship
634 between U and TOC content. This is because the U content of Silurian shales in North Africa,
635 measured by portable gamma-ray spectrometry (PGRS), is commonly taken as a proxy for the
636 TOC content of the sediment in the search for possible 'hot' shales (e.g., Lüning et al., 2003;
637 Lüning and Fello, 2008). Although this technique seems to work well in certain areas of
638 North Africa and Arabia, especially for samples with high TOC content, there are a number of
639 facts to consider regarding the actual potential sources of U in sedimentary rocks.
640 The most important source of U is dissolved U carried from the world's rivers to the
641 oceans. As already mentioned above, this source of U can be removed from ocean water by
642 diffusion across the sediment-water interface and eventual reduction may lead to the residence
643 in organic-rich shales (Klinkhammer and Palmer, 1991; Brumsack, 2006). This form of U is

644 called authigenic U. Changes of the U concentration in sediment with time are controlled
645 primarily by the U concentration of the source material settling from the water column, and
646 secondarily, by the organic content of this material and the sedimentation rate (Klinkhammer
647 and Palmer, 1991). This process is so effective that about 75% of the U being supplied to the
648 oceans is being removed by diffusion into suboxic sediments (Klinkhammer and Palmer,
649 1991). Thus, U is considered as being associated with the organic matter in the sediment
650 rather than the clay minerals. Yet, in marine sediments organic matter seems to be associated
651 with different types of clay minerals due to processes of adsorption and entrapment (e.g.,
652 Bader et al., 1960; Bishop and Philp, 1994, and references therein) and therefore U may be
653 indirectly related to clay minerals as well (see also Chabaux et al., 2003). In addition, U may
654 be enriched in sediment due to the accumulation of zircon as a major carrier of U. For
655 example, zircon could be concentrated in heavy mineral sands (placer deposits). Uranium may
656 also be enriched through U mineralisation. One example is the Upper Palaeozoic and Lower
657 Mesozoic continental sedimentary succession in the Aïr mountains of Niger (e.g., Bowden et
658 al., 1981). Uranium was derived from igneous rocks and their eroded cover and was
659 consequently concentrated in the sediment matrix and on secondary Fe-oxide coatings
660 surrounding lithic and crystal fragments (Bowden et al., 1981).
661 Thus, there is one major and at least three other potential sources of U in sedimentary
662 rocks. Alternatives to the common association of U with organic matter seem to have been
663 overlooked in the studies of the North Africa Silurian shales. Klinkhammer and Palmer
664 (1991) addressed the subject of U source in sediment and its mobilisation thoroughly. Further
665 research is needed to clarify the applicability of U concentrations as a tracer to detect ‘hot’
666 shales.
667

5. Conclusions

Elemental geochemistry of 47 shale samples from the latest Hirnantian–earliest Rhuddanian Tanezzuft Formation collected from the 20.80–73.21 m interval in borehole JA-2 clearly shows the mobility of individual trace elements related to surface weathering. For example, Mn is depleted and Sc is enriched in the weathered section. Throughout the core from 20.80 m to 67.59 m interval concentrations of U range between 3.1 and 5.3 ppm, while the deeper section (67.82–73.21 m) shows U contents between 6 and 12 ppm. TOC content do not correlate with U concentrations. For example, the highest TOC of 0.75 wt% (HI = 187 mg S_2/ g TOC) is associated with a U value of 4.7 ppm. Moreover, the highest U value of 11.9 ppm corresponds to an intermediate TOC value of only 0.46 wt% (HI = 246 mg S_2/g TOC). This observation demonstrates that the correlation between U and TOC may break down at low TOC and U contents and organic matter is not the only source for U accumulation in sediments. Therefore, total U contents determined with portable gamma-ray spectrometry (PGRS) at outcrop may not always reflect the TOC content of the sediment.

Calculated whole-rock Ce anomalies of the analysed shale samples fluctuate around 0.93, which suggests no significant change in redox conditions throughout the cored section, except perhaps at depths of 55.53 m and 73.20 m where the Ce-anomaly values are 0.78 and 1.08 respectively.

The positive correlation between Rb and K_2O suggests that Rb is fixed in K-feldspar since K_2O correlates positively with the K-feldspar content. In general, quartz, K-feldspar, kaolinite and illite form the prominent mineral assemblage. Chlorite, siderite and pyrite are also present in many samples but only in minor amounts. Kaolinite/illite and K-feldspar/quartz ratios are increasing and decreasing, respectively, from about 65 m depth

towards the base of the core. Although Rb correlates positively with the K-feldspar content, it shows a much better positive correlation with the illite content. Therefore, illite and minor K-feldspar is likely the carrier of Rb in the JA-2 sediments. The negative correlation between Rb and Sr reflects the different behaviour of Rb and Sr during chemical weathering. High Sr and low Rb contents (plus Rb/Sr < 1) in the highly weathered section (Th/K > 9), in the deepest part of the JA-2 core are accompanied by high kaolinite contents (>35 %) and high kaolinite/illite ratios (>1.5). This significant change in whole-rock geochemical composition and mineralogy is also reflected in a dramatic drop of the abundance of the chitinozoans (Thusu et al., 2013), possibly related to oxidation noticed on the core samples. Therefore, elevated U concentrations (>6 ppm) of samples from this part of the core are likely related to intensive chemical weathering due to humid and warm palaeo-climate. A temporary emersion event may have occurred during the lastest Hirnantian–earliest Rhuddanian post-glacial rebound, which resulted in the weathering of older strata. Groundwater circulation in a small fault as observed in the lower part of the core also has the potential to generate the oxidation of the sediment and of its organic matter in the deeper part of the core. This faulting may be synsedimentary as this part of the core should be near the base of the Tanezzuft Formation and there is a lot of post-depositional remobilisation of the Mamuniyat Formation into the Tanezzuft Formation in the vicinity (CASP unpublished data).

The present study clearly demonstrates that the relationship between the content of total organic carbon (TOC) and the actinide metal uranium is more complex for latest Hirnantion to Rhuddanian shales than currently assumed. This may limit the use of the U content, determined by PGRS at outcrop (particularly at low concentrations of U and TOC), to identify potential ‘hot’ shales in Libya or elsewhere. Thus, there is clearly the need for

715 further investigations to address this subject, which may help developing new models for
716 'hot' shales deposition.
717
718 **Declaration of competing interest**
719
720 The authors have no conflicts of interest to declare.
721
722 **Acknowledgements**
723
724 This research was carried out as part of CASP's Kufra Basin Project. Our sponsors' financial
725 support is gratefully acknowledged. We thank Faraj Said (National Oil Corporation, Tripoli,
726 Libya), Ahmed I. Asbali (Arabian Gulf Oil Company, Benghazi, Libya), Ramadan Aburawi
727 and Bourima Belgasem (Libyan Petroleum Institute, Tripoli, Libya) for their support and
728 guidance during the project work in Libya. We thank the logistics team, provided by Bashir
729 Grenat, for assistance in the field. The administrative and logistical support of staff at the
730 Libyan Petroleum Institute is gratefully acknowledged. Our special thanks go to James
731 Stewart and Clive Johnson for their support during the drilling campaign in Libya and to
732 Jason Day, Sally Gibson and Richard Pearson for analytical support with geochemical and X-
733 ray diffraction analyses, respectively. The manuscript benefited from thoughtful reviews by
734 two anonymous reviewers.
735
736 **Appendix A. Supplementary data**
737
738 Supplementary data to this article can be found online at https://doi.org/xxxxxx

References

Abohajar, A., Littke, R., Schwarzbauer, J., Weniger, P., Boote, D.R.D., 2015. Biomarker characteristics of potential source rocks in the Jabal Nafusah area, NW Libya: Petroleum systems significance. Journal of Petroleum Geology 38, 119–156. https://doi.org/10.1111/jpg.12603.

Bader, R.G., Hood, D.W., Smith, J.B., 1960. Recovery of dissolved organic matter in seawater and organic sorption by particulate material. Geochimica et Cosmochimica Acta 19, 236–243. https://doi.org/10.1016/0016-7037(60)90031-4.

Bateman, R.M., 1985. Open-hole log analysis and formation evaluation. International Human Resources Development Corporation, Boston, 647 pp.

Bishop, A.N., Philp, R.P., 1994. Potential for amorphous kerogen formation via adsorption of organic material at mineral surfaces. Energy & Fuels 8, 1494–1497. https://doi.org/10.1021/ef00048a040.

Bowden, P., Bennett, J.N., Kinnaird, J.A., Whitley, J.E., Abaa, S.I., Hadzigeorgiou-Stavrakis, P.K., 1981. Uranium in the Niger–Nigeria Younger Granite Province. Mineralogical Magazine 44, 379–389.

Brumsack, H.-J., 2006. The trace metal content of recent organic carbon-rich sediments: Implications for Cretaceous black shale formation. Palaeogeography, Palaeoclimatology, Palaeoecology 232, 344–361. https://doi.org/10.1016/j.palaeo.2005.05.011.

Chabaux, F., Riotte, J., Dequincey, O., 2003. U–Th–Ra fractionation during weathering and river transport. In: Bourdon, B., Henderson, G.M., Lundstrom, C.C., Turner, S.P. (Eds.),

Uranium-series Geochemistry. Reviews in Mineralogy and Geochemistry, vol. 52, pp. 533–576. https://doi.org/10.2113/0520533.

De Baar, H.J.W., Bacon, M.P., Brewer, P.G., 1983. Rare-earth distribution with a positive Ce anomaly in the Western North Atlantic Ocean. Nature 301, 324–327. https://doi.org/10.1038/301324a0.

Dymond, J., Suess, E., Lyle, M., 1992. Barium in deep-sea sediment: A geochemical proxy for paleoproductivity. Paleoceanography 7, 163–181. https://doi.org/10.1029/92PA00181.

El Diasty, W.Sh., El Beialy, S.Y., Anwari, T.A., Batten, D.J., 2017a. Hydrocarbon source potential of the Tanezzuft Formation, Murzuq Basin, south-west Libya: An organic geochemical approach. Journal of African Earth Sciences 130, 102–109. https://doi.org/10.1016/j.jafrearsci.2017.03.005.

El Diasty, W.Sh., El Beialy, S.Y., Anwari, T.A., Peters, K.E., Batten, D.J., 2017b. Organic geochemistry of the Silurian Tanezzuft Formation and crude oils, NC115 Concession, Murzuq Basin, southwest Libya. Marine and Petroleum Geology 86, 367–385. https://doi.org/10.1016/j.marpetgeo.2017.06.002.

El Diasty, W.Sh., El Beialy, S.Y., Fadeel, F.I., Peters, K.E., Batten, D.J., 2017c. Organic geochemistry of the Lower Silurian Tanezzuft Formation and biomarker characteristics of crude oils from the Ghadames Basin, Libya. Journal of Petroleum Geology 40, 299–318. https://doi.org/10.1111/jpg.12677.

Elderfield, H., 1988. The oceanic chemistry of rare-earth elements. Philosophical Transactions of the Royal Society of London A 325, 105–126. https://doi.org/10.1098/rsta.1988.0046.

785 Elderfield, H., Greaves, M.J., 1982. The rare earth elements in seawater. Nature 296, 214–
786 219. https://doi.org/10.1038/296214a0.
787 Fello, N., Lüning, S., Storch, P., Redfern, J., 2006. Identification of early Llandovery
788 (Silurian) anoxic palaeo-depressions at the western margin of the Murzuq Basin
789 (southwest Libya), based on gamma-ray spectrometry in surface exposures. GeoArabia
790 11, 101–118.
791 Gindre, L., Le Heron, D., Morten Bjørnseth, H., 2012. High resolution facies analysis and
792 sequence stratigraphy of the Siluro-Devonian succession of Al Kufrah basin (SE Libya).
793 Journal of African Earth Sciences 76, 8–26.
794 https://doi.org/10.1016/j.jafrearsci.2012.08.002.
795 Guo, Q., Shields, G.A., Liu, C., Strauss, H., Zhu, M., Pi, D., Goldberg, T., Yang, X., 2007.
796 Trace element chemostratigraphy of two Ediacaran–Cambrian successions in South
797 China: Implications for organosedimentary metal enrichment and silicification in the
798 Early Cambrian. Palaeogeography, Palaeoclimatology, Palaeoecology 254, 194–216.
799 https://doi.org/10.1016/j.palaeo.2007.03.016.
800 Holser, W.T., 1997. Evaluation of the application of rare-earth elements to paleoceanography.
801 Palaeogeography, Palaeoclimatology, Palaeoecology 132, 309–323.
802 https://doi.org/10.1016/S0031-0182(97)00069-2.
803 Jin, Z., Cao, J., Wu, J., Wang, S., 2006. A Rb/Sr record of catchment weathering response to
804 Holocene climate change in Inner Mongolia. Earth Surface Processes and Landforms 31,
805 285–291. https://doi.org/10.1002/esp.1243.
806 Jin, Z., Wang, S., Shen, J., Zhang, E., Li, F., Ji, J., Lu, X., 2001. Chemical weathering since
807 the Little Ice Age recorded in lake sediments: A high-resolution proxy of past climate.
808 Earth Surface Processes and Landforms 26, 775–782. https://doi.org/10.1002/esp.224.

809 Jones, B., Manning, D.A.C., 1994. Composition of geochemical indices used for the
810 interpretation of paleoredox conditions in ancient mudstones. Chemical Geology 111,
811 111–129. https://doi.org/10.1016/0009-2541(94)90085-X.
812 Kabata-Pendias, A., Mukherjee, A.B., 2007. Trace elements from soil to human. Springer,
813 Berlin Heidelberg, 550 pp.
814 Klinkhammer, G.P., Palmer, M.R., 1991. Uranium in the oceans: Where it goes and why?
815 Geochimica et Cosmochimica Acta 55, 1799–1806. https://doi.org/10.1016/0016-
816 7037(91)90024-Y.
817 Le Heron, D.P., Armstrong, H.A., Wilson, C., Howard, J.P., Gindre, L., 2010. Glaciation and
818 deglaciation of the Libyan Desert: The Late Ordovician record. Sedimentary Geology
819 223, 100–125. https://doi.org/10.1016/j.sedgeo.2009.11.002.
820 Le Heron, D.P., Craig, J., Etienne, J.L., 2009. Ancient glaciations and hydrocarbon
821 accumulations in North Africa and the Middle East. Earth-Science Reviews 93, 47–76.
822 https://doi.org/10.1016/j.earscirev.2009.02.001.
823 Le Heron, D.P., Meinhold, G., Elgadry, M., Abutarruma, Y., Boote, D., 2015. Early
824 Palaeozoic evolution of Libya: perspectives from Jabal Eghei with implications for
825 hydrocarbon exploration in Al Kufrah Basin. Basin Research 27, 60–83.
826 https://doi.org/10.1111/bre.12057.
827 Le Heron, D.P., Meinhold, G., Page, A., Whitham, A., 2013. Did lingering ice sheets
828 moderate anoxia in the Early Palaeozoic of Libya? Journal of the Geological Society 170,
829 327–339. https://doi.org/10.1144/jgs2012-108.
830 Loydell, D., Butcher, A., Fryda, J., 2013. The middle Rhuddanian (lower Silurian) ‘hot’ shale
831 of North Africa and Arabia: an atypical hydrocarbon source rock. Palaeogeography,

Palaeoclimatology, Palaeoecology 386, 233–256. https://doi.org/10.1016/j.palaeo.2013.05.027.

Lüning, S., Fello, N., 2008. Silurian 'hot shales' in the Murzuq and Al Kufrah Basins (S Libya): Improved predictability of source rock distribution based on gamma-ray spectrometry in surface exposures. In: Salem, M.J., Oun, K.M. and Essed, A.S. (Eds.), The Geology of East Libya. Sedimentary Basins of Libya – Third Symposium, Vol. 4, Gutenberg Press Ltd, Malta, pp. 3–12.

Lüning, S., Kolonic, S., 2003. Uranium spectral gamma-ray response as a proxy for organic richness in black shales: Applicability and limitations. Journal of Petroleum Geology 26, 153–174. https://doi.org/10.1111/j.1747-5457.2003.tb00023.x.

Lüning, S., Kolonic, S., Loydell, D., Craig, J., 2003. Reconstruction of the original organic richness in weathered Silurian shale outcrops (Murzuq and Kufra basins, southern Libya). GeoArabia 8, 299–308.

Lüning, S., Craig, J., Fitches, B., Gamudi, A., Mayouf, J., Busrewil, A., El Dieb, M., Loydell, D., McIlroy, D., 1999. Re-evaluation of the petroleum potential of the Kufra Basin (SE Libya, NE Chad): does the source rock barrier fall? Marine and Petroleum Geology 16, 693–718. https://doi.org/10.1016/S0264-8172(99)00013-6.

Lüning, S., Craig, J., Loydell, D.K., Štorch, P., Fitches, B., 2000. Lower Silurian 'hot shales' in North Africa and Arabia: regional distribution and depositional model. Earth-Science Reviews 49, 121–200. https://doi.org/10.1016/S0012-8252(99)00060-4.

McLennan, S.M., 1989. Rare earth elements in sedimentary rocks: influence of provenance and sedimentary processes. In: Lipin, B.R., McKay, G.A. (Eds.), Geochemistry and Mineralogy of Rare Earth Elements. Reviews in Mineralogy 21, 170–199. https://doi.org/10.1515/9781501509032-010.

McLennan, S.M., Hemming, S., McDaniel, D.K., Hanson, G.N., 1993. Geochemical approach to sedimentation, provenance and tectonics. In: Johnsson, M.J., Basu, A. (Eds.), Processes controlling the composition of clastic sediments. Geological Society of America, Special Paper 285, 21–40. https://doi.org/10.1130/SPE284-p21.

MacLeod, K.G., Irving, A.J., 1996. Correlation of cerium anomalies with indicators of paleoenvironment. Journal of Sedimentary Reseach 66, 948–955. https://doi.org/10.1306/D426844B-2B26-11D7-8648000102C1865D.

McManus, J., Berelson, W.M., Klinkhammer, G.P., Johnson, K.S., Coale, K.H., Anderson, R.F., Kumar, N., Burdige, D.J., Hammond, D.E., Brumsack, H.J., McCorkle, D.C., Rushdi, A., 1998. Geochemistry of barium in marine sediments: Implications for its use as a paleoproxy. Geochimica et Cosmochimica Acta 62, 3453–3473. https://doi.org/10.1016/S0016-7037(98)00248-8.

Meinhold, G., 2010. Rutile and its applications in earth sciences. Earth-Science Reviews 102, 1–28. https://doi.org/10.1016/j.earscirev.2010.06.001.

Meinhold, G., Howard, J.P., Strogen, D., Kaye, M.D., Abutarruma, Y., Elgadry, M., Thusu, B., Whitham, A.G., 2013a. Hydrocarbon source rock potential and elemental composition of lower Silurian subsurface shales of the eastern Murzuq Basin, southern Libya. Marine and Petroleum Geology 48, 224–246. https://doi.org/10.1016/j.marpetgeo.2013.08.010.

Meinhold, G., Le Heron, D.P., Elgadry, M., Abutarruma, Y., 2016. The search for “hot shales” in the western Kufra Basin, Libya: Geochemical and mineralogical characterisation of outcrops, and insights into latest Ordovician climate. Arabian Journal of Geosciences 9, article number: 62. https://doi.org/10.1007/s12517-015-2173-0.

879 Meinhold, G., Morton, A.C., Fanning, C.M., Frei, D., Howard, J.P., Phillips, R.J., Strogen, D.
880 and Whitham, A.G., 2011. Evidence from detrital zircons for recycling of
881 Mesoproterozoic and Neoproterozoic crust recorded in Paleozoic and Mesozoic
882 sandstones of southern Libya. Earth and Planetary Science Letters 312, 164–175. https://
883 doi.org/10.1016/j.epsl.2011.09.056.
884 Meinhold, G., Whitham, A.G., Howard, J.P., Stewart, J.C., Abutarruma, Y., Thusu, B., 2013b.
885 Hydrocarbon source rock potential of latest Ordovician–earliest Silurian Tanezzuft
886 Formation shales from the eastern Kufra Basin, SE Libya. Journal of Petroleum Geology
887 36, 105–116. https://doi.org/10.1111/jpg.12546.
888 Möller, P., Dulski, P., Bau, M., 1994. Rare-earth element adsorption in a seawater profile
889 above the East Pacific Rise. Chemie der Erde 54, 129–149.
890 Murray, R.W., Buchholtz ten Brink, M.R., Jones, D.L., Gerlach, D.C., Russ, G.P. III, 1990.
891 Rare earth element as indicators of different marine depositional environments in chert
892 and shale. Geology 18, 268–271. https://doi.org/10.1130/0091-
893 7613(1990)018<0268:REEAIO>2.3.CO;2.
894 Nance, W.B., Taylor, S.R., 1976. Rare earth element patterns and crustal evolution—I.
895 Australian post-Archean sedimentary rocks. Geochimica et Cosmochimica Acta 40,
896 1539–1551. https://doi.org/10.1016/0016-7037(76)90093-4.
897 Page, A.A., Meinhold, G., Le Heron, D.P., Elgadry, M., 2013. *Normalograptus kufraensis*, a
898 new species of graptolite from the western margin of the Kufra Basin, Libya. Geological
899 Magazine 150, 743–755. https://doi.org/10.1017/S0016756812000787.
900 Paris, F., Thusu, B., Rasul, S., Meinhold, G., Strogen, D., Howard, J.P., Abutarruma, Y.,
901 Elgadry, M., Whitham, A.G., 2012. Palynological and palynofacies analysis of early
902 Silurian shales from borehole CDEG-2a in Dor el Gussa, eastern Murzuq Basin, Libya.

Review of Palaeobotany and Palynology 174, 1–26. https://doi.org/10.1016/j.revpalbo.2012.02.002.

Pattan, J.N., Pearce, N.J.G. and Mislankar, P.G., 2005. Constraints in using Cerium-anomaly of bulk sediments as an indicator of paleo bottom water redox environment: A case study from the Central Indian Ocean Basin. Chemical Geology 221, 260–278. https://doi.org/10.1016/j.chemgeo.2005.06.009.

Ringwood, A.E., 1955. The principles governing trace element distribution during magmatic crystallization Part I: The influence of electronegativity. Geochimica et Cosmochimica Acta 7, 189–202. https://doi.org/10.1016/0016-7037(55)90029-6.

Stockey, R.G., Cole, D.B., Planavsky, N.J., Loydell, D.K., Frýda, J., Sperling, E.A., 2020. Persistent global marine euxinia in the early Silurian. Nature Communications 11, 1804. https://doi.org/10.1038/s41467-020-15400-y.

Sutcliffe, O.E., Dowdeswell, J.A., Whittington, R.J., Theron, J.N., Craig, J., 2000. Calibrating the Late Ordovician glaciation and mass extinction by the eccentricity cycles of Earth's orbit. Geology 28, 967–970. https://doi.org/10.1130/0091-7613(2000)28<967:CTLOGA>2.0.CO;2.

Taylor, S.R., McLennan, S.M., 1985. The Continental Crust: its Composition and Evolution. Blackwell, Oxford, 307 pp.

Thusu, B., Rasul, S., Paris, F., Meinhold, G., Howard, J.P., Abutarruma, Y., Whitham, A.G., 2013. Latest Ordovician–earliest Silurian acritarchs and chitinozoans from subsurface samples in Jebel Asba, Kufra Basin, SE Libya. Review of Palaeobotany and Palynology 197, 90–118. https://doi.org/10.1016/j.revpalbo.2013.05.006.

925 Turner, B.R., 1980. Palaeozoic sedimentology of the southeastern part of Al Kufrah Basin,
926 Libya: A model for oil exploration. In: Salem, M.J., Busrewil, M.T. (Eds.) The Geology
927 of Libya, Vol. 2. Academic Press, London, 351-374.
928 Vecoli, M., Riboulleau, A., Versteeg, G.J.M., 2009. Palynology, organic geochemistry and
929 carbon isotope analysis of a latest Ordovician through Silurian clastic succession from
930 borehole Tt1, Ghadamis Basin, southern Tunisia, North Africa: palaeoenvironmental
931 interpretation. Palaeogeography Palaeoclimatology Palaeoecology 273, 378–394. https://
932 doi.org/10.1016/j.palaeo.2008.05.015.
933 Wignall, P.B., Myers, K.J., 1988. Interpreting the benthic oxygen levels in mudrocks, a new
934 approach. Geology 16, 452–455. https://doi.org/10.1130/0091-
935 7613(1988)016<0452:IBOLIM>2.3.CO;2.
936 Wignall, P.B., Twitchett, R.J., 1996. Oceanic anoxia and the end Permian mass extinction.
937 Science 272, 1155–1158. https://doi.org/10.1126/science.272.5265.1155.
938 Wilde, P., Quinby-Hunt, M.S., Erdtmann, B.D., 1996. The whole-rock cerium anomaly: a
939 potential indicator of eustatic sealevel changes in shales of the anoxic facies.
940 Sedimentary Geology 101, 43–53. https://doi.org/10.1016/0037-0738(95)00020-8.
941
942 **Figure captions**
943
944 **Fig. 1.** Geological map of Libya and neighbouring countries showing location of the Kufra
945 Basin in SE Libya (after Meinhold et al., 2011). The location of the borehole JA-2 in southern
946 Jebel Asba at the eastern margin of the Kufra Basin (Meinhold et al., 2013b; this study) and
947 of the borehole CDEG-2a at the eastern margin of the Murzuq Basin (Paris et al., 2012;
948 Meinhold et al., 2013a) are indicated.
949
950 **Fig. 2.** Generalized stratigraphic column for Upper Ordovician–ower Silurian strata in Jebel
951 Asba in SE Libya, with main lithologies, thicknesses, and depositional environment (modified

after Meinhold et al., 2013b). It is referred to Gindre et al. (2012) for details about the sedimentology and facies analysis.

Fig. 3. Landsat image (NASA Landsat Program) of southern Jebel Asba in SE Libya with the distribution of Tanezzuft Formation shales superimposed and the location of the borehole JA-2 (modified after Meinhold et al., 2013b).

Fig. 4. Summary of the stratigraphic distribution of selected source rock data, trace element concentrations, mineralogical composition and of palynological and kerogen parameters in shales from borehole JA-2 in southern Jebel Asba, SE Kufra Basin. The lithology, bulk gamma-ray log, total organic carbon (TOC) and hydrogen index (HI) values were taken from Meinhold et al. (2013a), the uranium (U) values and mineralogical composition are from this study, and the chitinozoan abundance and kerogen data are from Thusu et al. (2013). Palynological examination of samples suggest that the unweathered section belongs to the *Euconochitina moussegoudaensis*/*Spinachitina oulebsiri* Chitinozoan Zone (Thusu et al., 2013). Note that only 0.5 m of casing was retrieved; the rest had fallen into the borehole. The deflection of the shale line to the left between 20 and ~32 m indicates the position of the fallen section of casing (marked with a red arrow).

Fig. 5. Stratigraphic distribution of selected trace element concentrations and of palaeoenvironmental sensitive parameters in shales from borehole JA-2 in southern Jebel Asba, SE Kufra Basin. The TOC and HI values were taken from Meinhold et al. (2013a).

Fig. 6. Stratigraphic distribution of selected trace element concentrations and element ratios in shales from borehole JA-2.

Fig. 7. Stratigraphic distribution of selected trace element concentrations and total REE in shales from borehole JA-2.

Fig. 8. Stratigraphic distribution of the REE concentrations in shales from borehole JA-2.

Fig. 9. (a, b) Total Organic Carbon (TOC) and Hydrogen Index (HI) versus U content cross plots for samples from borehole JA-2.

Fig. 10. (a, b) U and Hf contents versus Zr content for samples from borehole JA-2. (b) Hf and Zr are well correlated due to the resistance in zircon.

Fig. 11. (a, b) K_2O and Sr contents versus Rb content for samples from borehole JA-2. (a) K_2O and Rb are well correlated probably due to the resistance in K-feldspar.

Fig. 12. (a, b) Rb/Sr and Th/K contents versus U content for samples from borehole JA-2.

Fig. 13. (a) Nb versus TiO_2 cross plot. The positive correlation between Nb and TiO_2 suggests rutile as major source for Nb in the sediment. (b) Ni versus Co cross plot shows positive correlation between both elements with depletion of Ni and Co, respectively, in the weathered sections.

Fig. 14. REE diagrams for drill core from borehole JA-2. The samples are arranged with increasing depth. Samples in (a, b) come from the upper weathered section. Samples in (c–f) appear unweathered; organic matter is preserved. Samples in (g–l) come from the unweathered section; organic matter is preserved. In samples from 67.21 m to 67.97 m depths (m, n) organic matter is preserved, although the abundance is low in the sample from 67.97 m depth. Samples in (o, p) come from the lower weathered section; no organic matter is preserved.

Fig. 15. Stratigraphic distribution of the whole-rock content of selected minerals and mineral ratios in shales from borehole JA-2.

Fig. 16. (a) K-feldspar contents versus Th/K cross plot. (b) K-feldspar versus K_2O contents cross plot. The inset (c) shows the K-feldspar versus kaolinite contents cross plot.

Fig. 17. (a) A) K-feldspar versus Rb contents cross plot. The inset shows the negative correlation between the K-feldspar content and Th/K. (b) Illite versus Rb contents cross plot shows positive correlation between illite and Rb.

Fig. 18. (a) Sr versus K-feldspar/illite contents cross plot. (b) K-feldspar/quartz versus K-feldspar/illite contents cross plot.

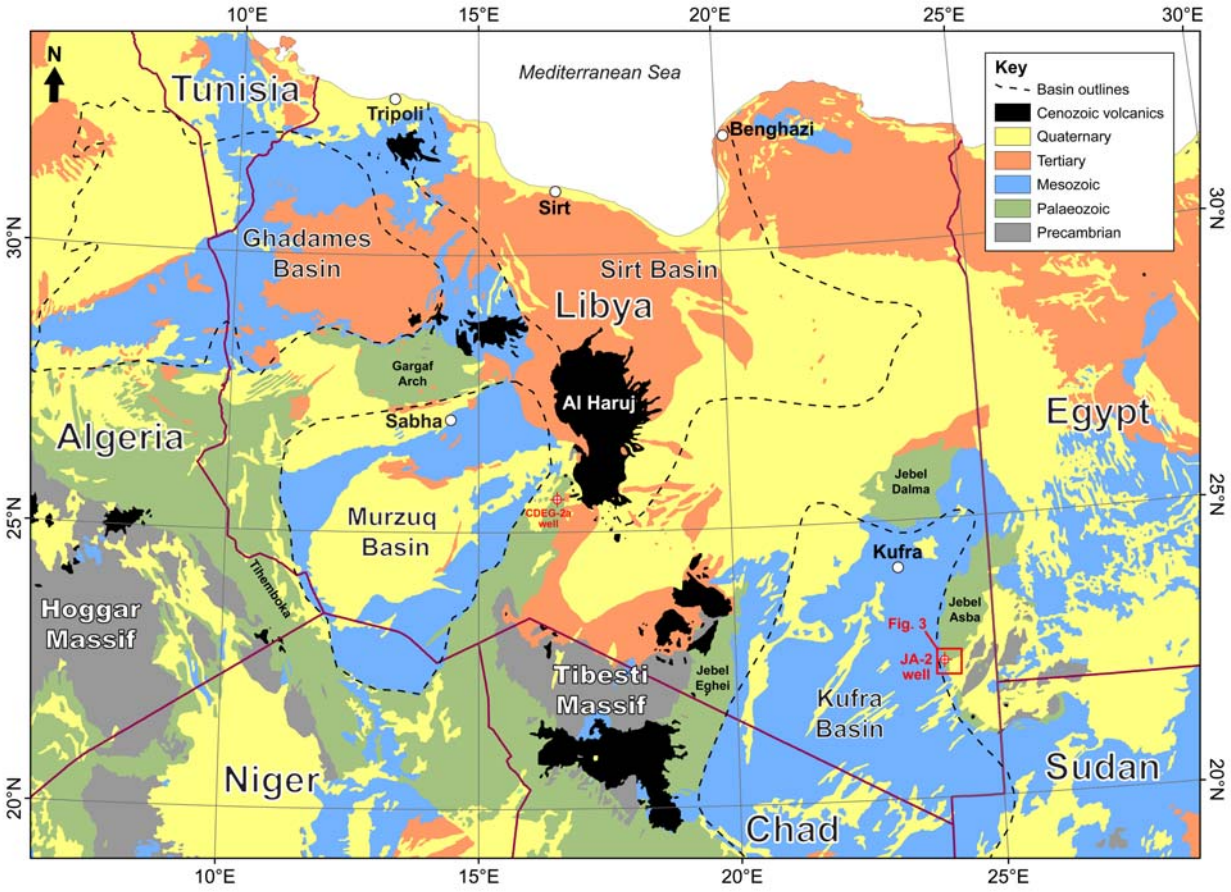

Figure 1

System	Series	Stage	Formation	Lithology	Thickness	Depositional environment
Silurian	Llandovery	Telychian	Akakus Formation	Sandstone	0–28 m	deltaic
		Aeronian				
		Rhuddanian	Tanezzuft Formation	Mudrock	0–78 m	offshore
Ordovician	Upper	Hirnantian	Mamuniyat Formation	Sandstone	>70 m	proglacial shelf
		Katian				
		Sandbian				

Figure 2

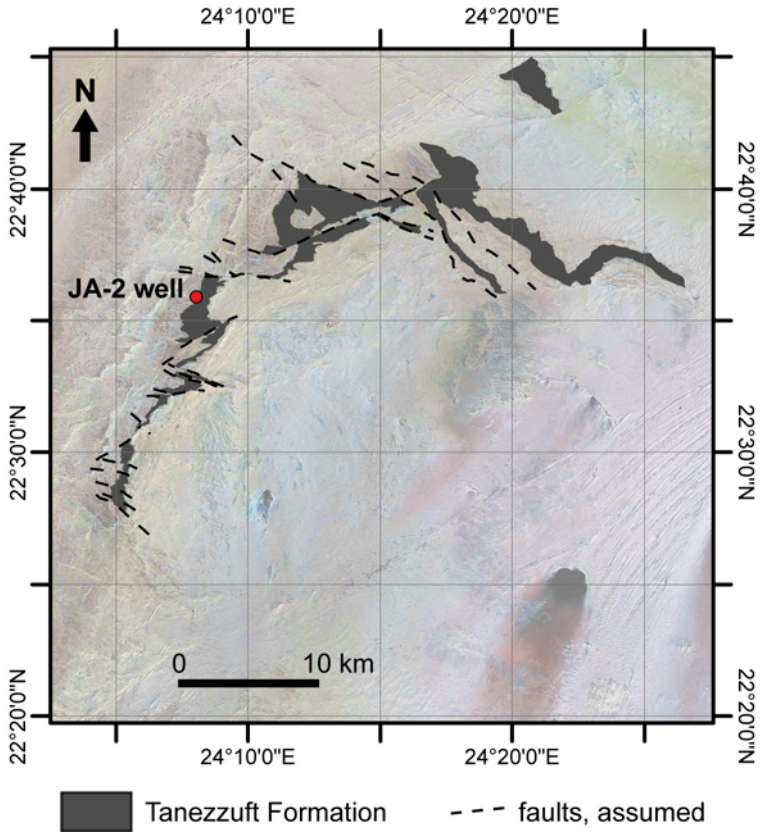

Figure 3

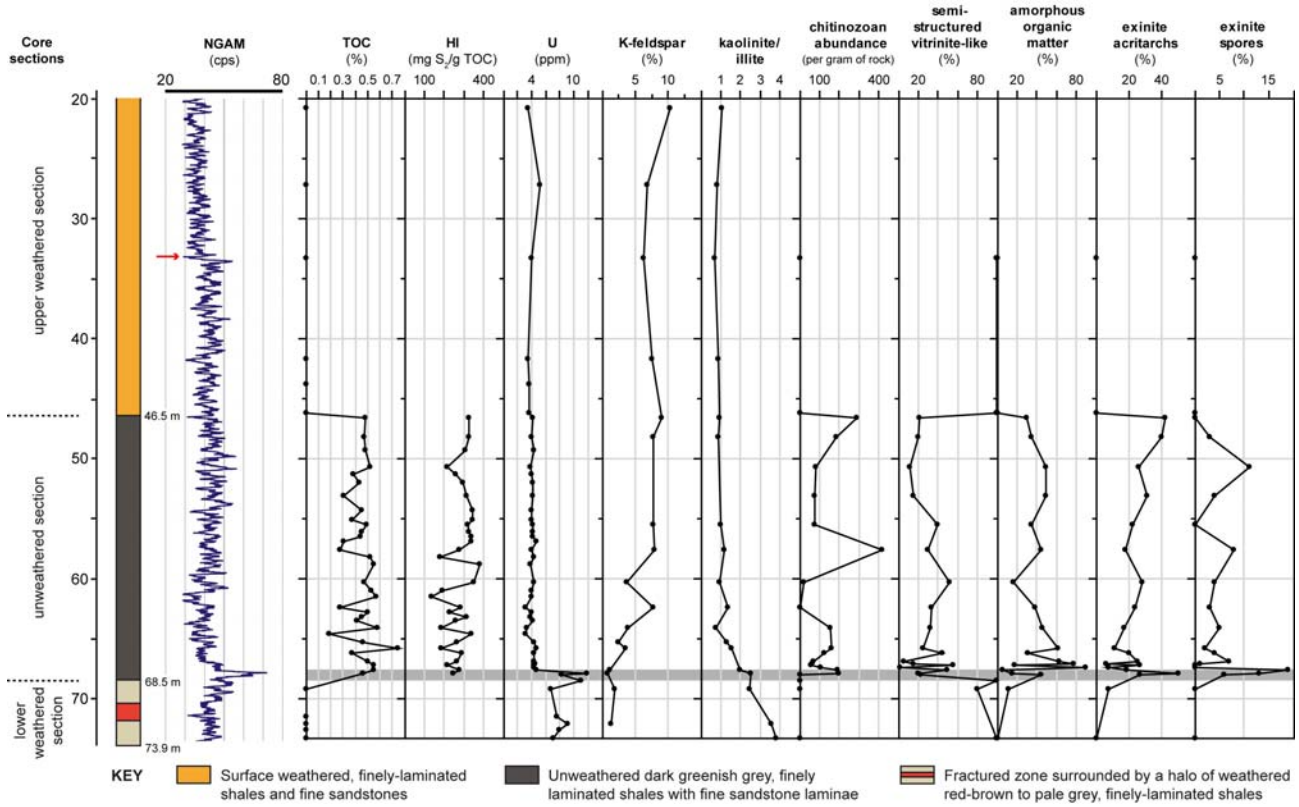

Figure 4

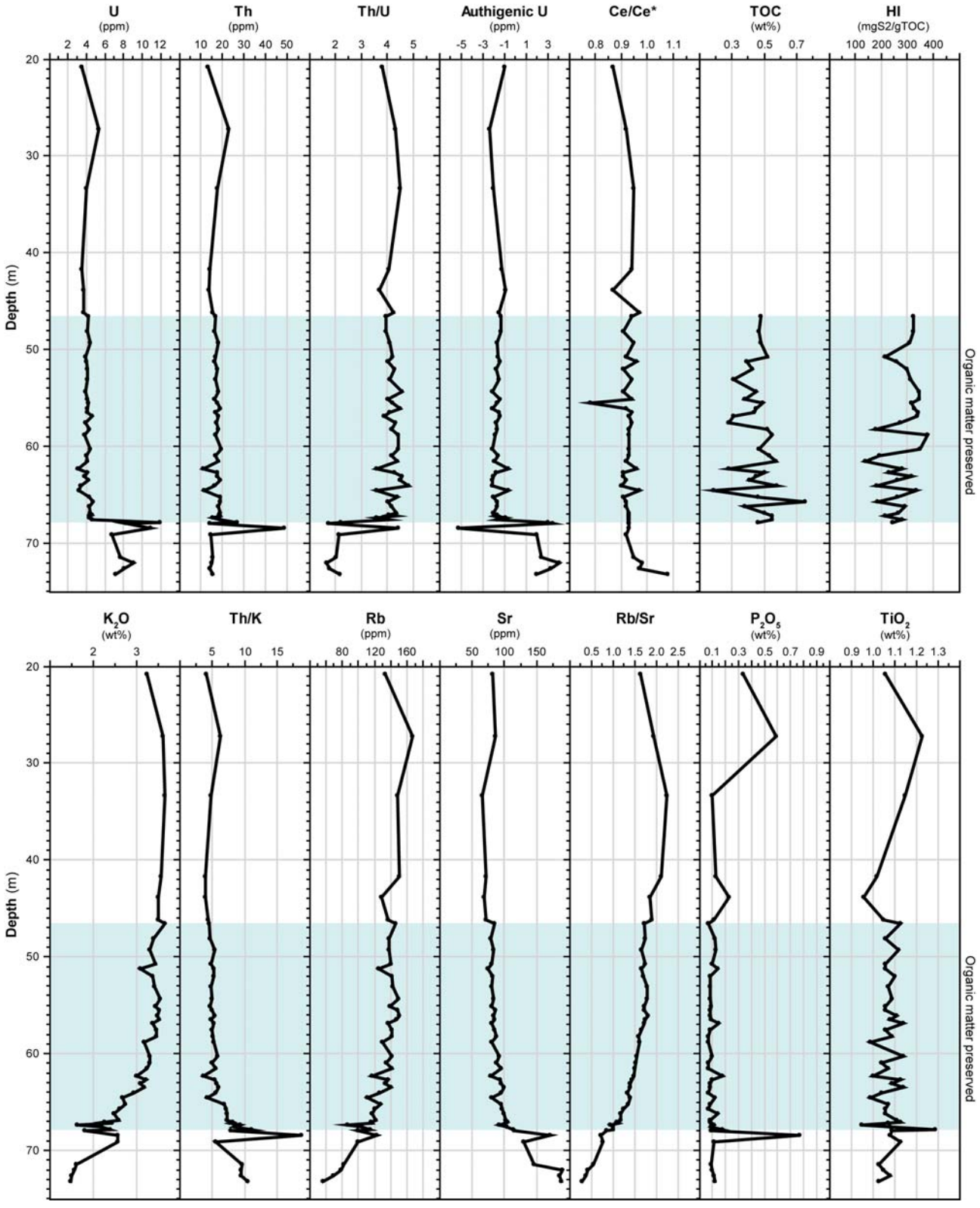
U
(ppm)
Th
(ppm)
Th/U
Authigenic U
(ppm)
Ce/Ce*
TOC
(wt%)
HI
(mgS2/gTOC)
Depth (m)
Organic matter preserved
K2O
(wt%)
Th/K
Rb
(ppm)
Sr
(ppm)
Rb/Sr
P2O5
(wt%)
TiO2
(wt%)
Depth (m)
Organic matter preserved

Figure 5

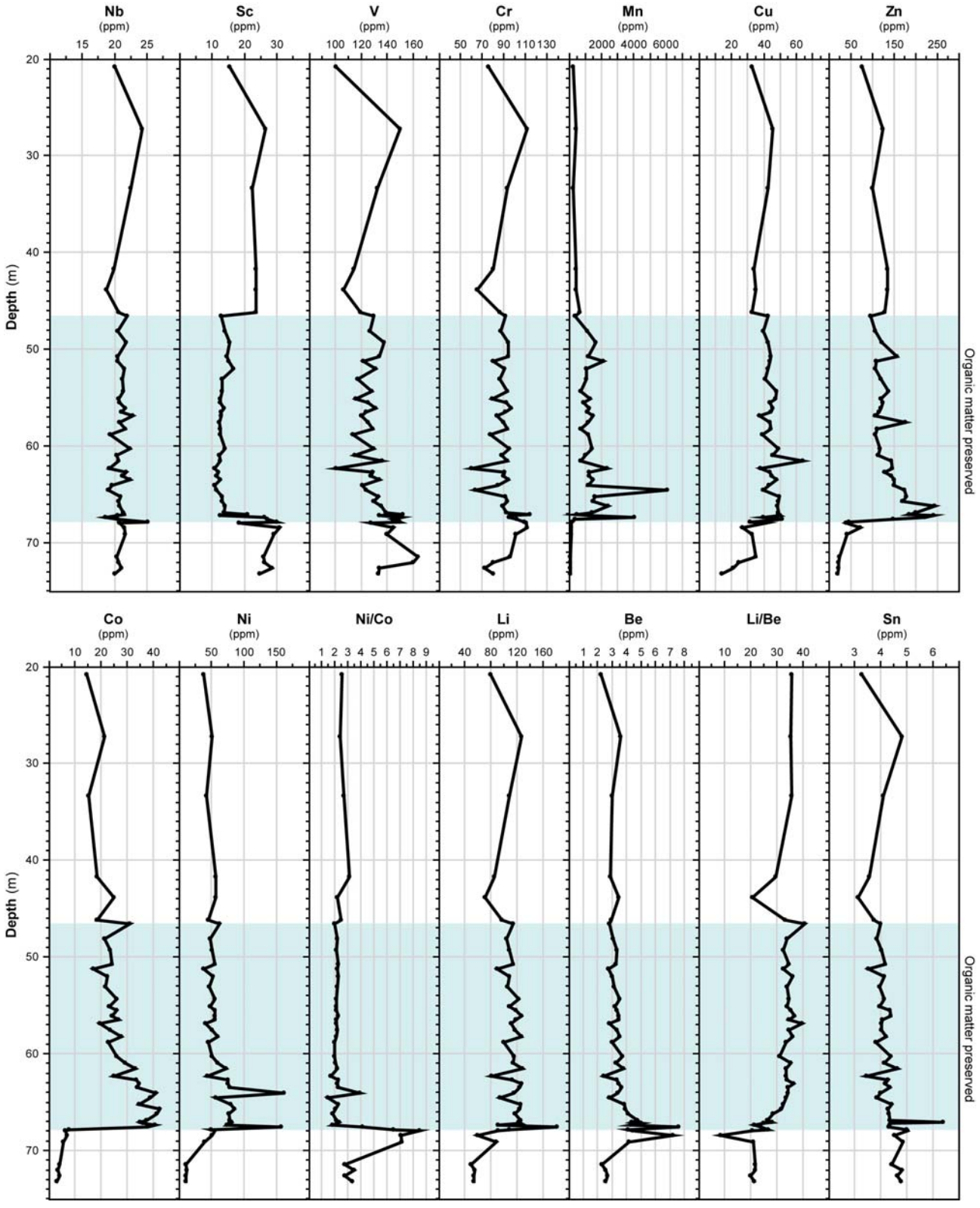
Nb (ppm)
Sc (ppm)
V (ppm)
Cr (ppm)
Mn (ppm)
Cu (ppm)
Zn (ppm)
Depth (m)
Organic matter preserved
Co (ppm)
Ni (ppm)
Ni/Co
Li (ppm)
Be (ppm)
Li/Be
Sn (ppm)
Depth (m)
Organic matter preserved

Figure 6

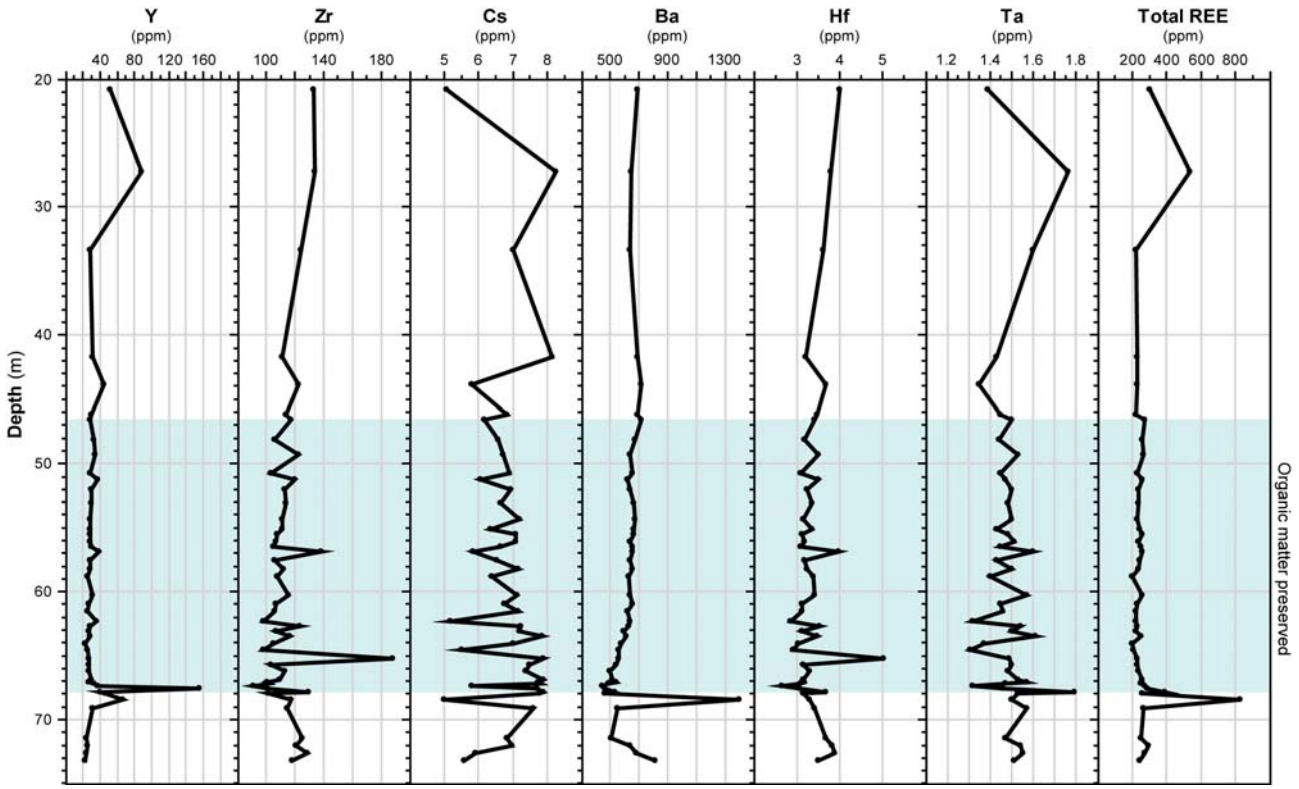

Figure 7

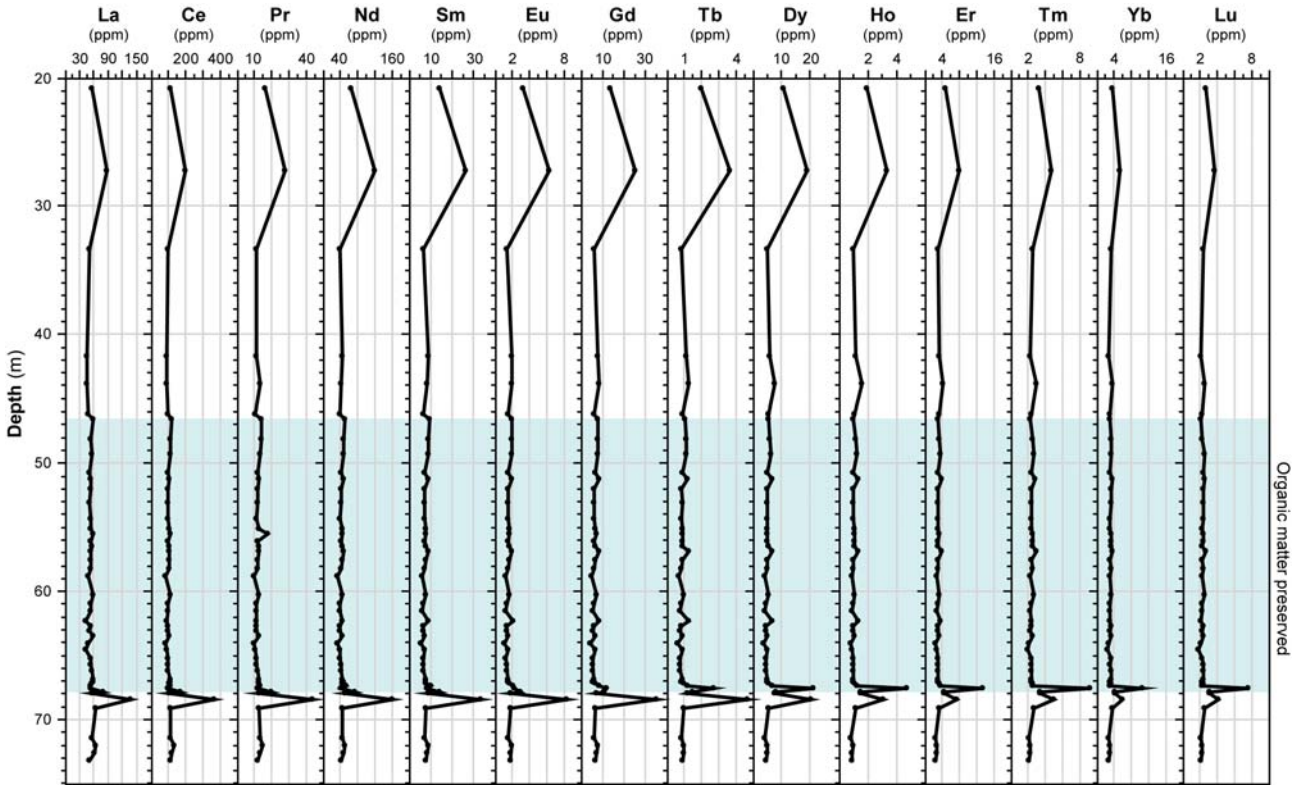

Figure 8

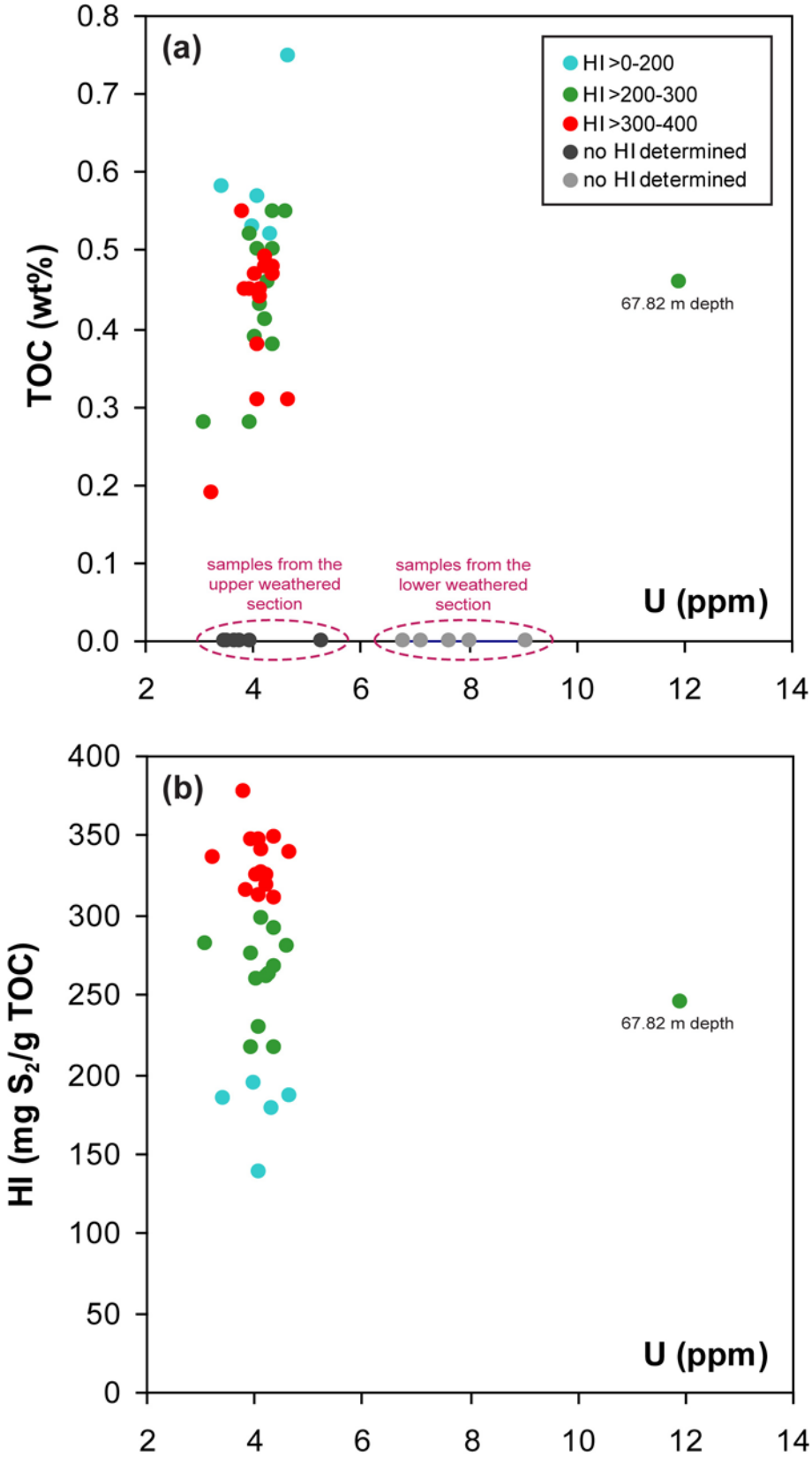
(a)
HI >0-200
HI >200-300
HI >300-400
no HI determined
no HI determined
67.82 m depth
samples from the upper weathered section
samples from the lower weathered section
TOC (wt%)
U (ppm)
0.0
0.1
0.2
0.3
0.4
0.5
0.6
0.7
0.8
2
4
6
8
10
12
14
(b)
67.82 m depth
HI (mg S2/g TOC)
U (ppm)
0
50
100
150
200
250
300
350
400

Figure 9

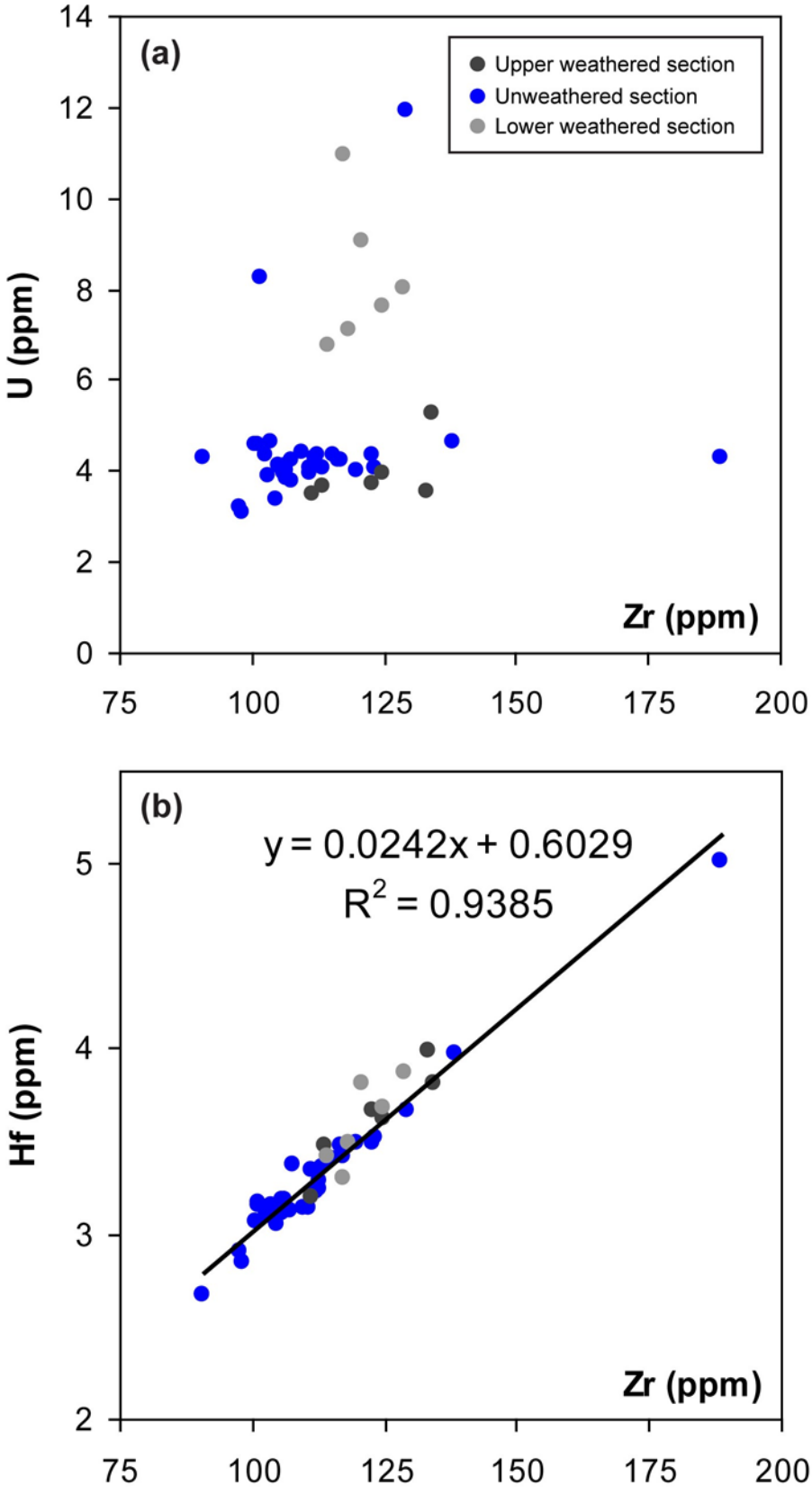
(a)
Upper weathered section
Unweathered section
Lower weathered section
U (ppm)
Zr (ppm)
0
2
4
6
8
10
12
14
75
100
125
150
175
200
(b)
y = 0.0242x + 0.6029
R2 = 0.9385
Hf (ppm)
Zr (ppm)
2
3
4
5
75
100
125
150
175
200

Figure 10

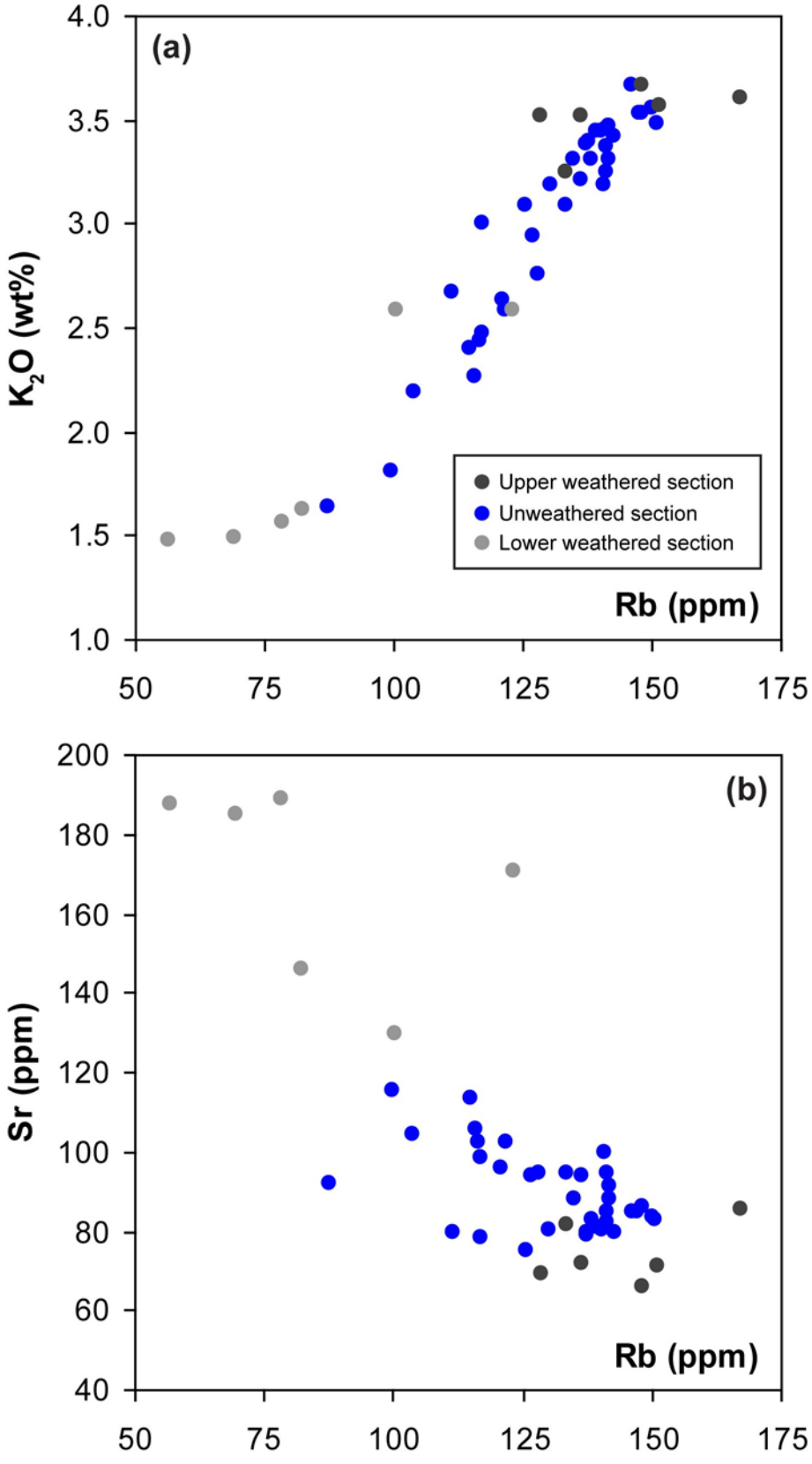
(a)
K_2O (wt%)
4.0
3.5
3.0
2.5
2.0
1.5
1.0
Upper weathered section
Unweathered section
Lower weathered section
Rb (ppm)
50
75
100
125
150
175
(b)
Sr (ppm)
200
180
160
140
120
100
80
60
40
Rb (ppm)
50
75
100
125
150
175

Figure 11

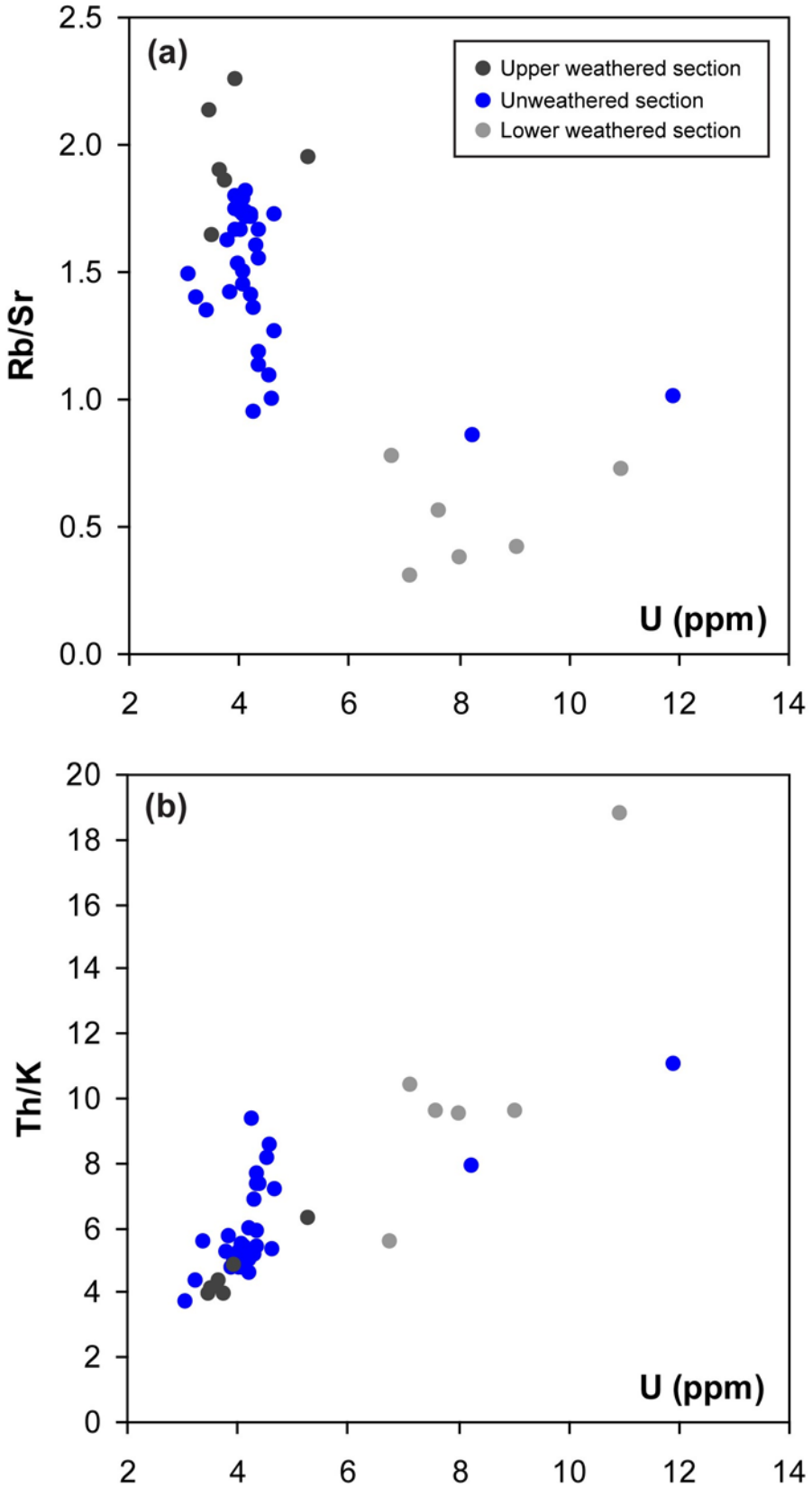
(a)
Upper weathered section
Unweathered section
Lower weathered section
Rb/Sr
U (ppm)
2.5
2.0
1.5
1.0
0.5
0.0
2
4
6
8
10
12
14
(b)
Th/K
U (ppm)
20
18
16
14
12
10
8
6
4
2
0

Figure 12

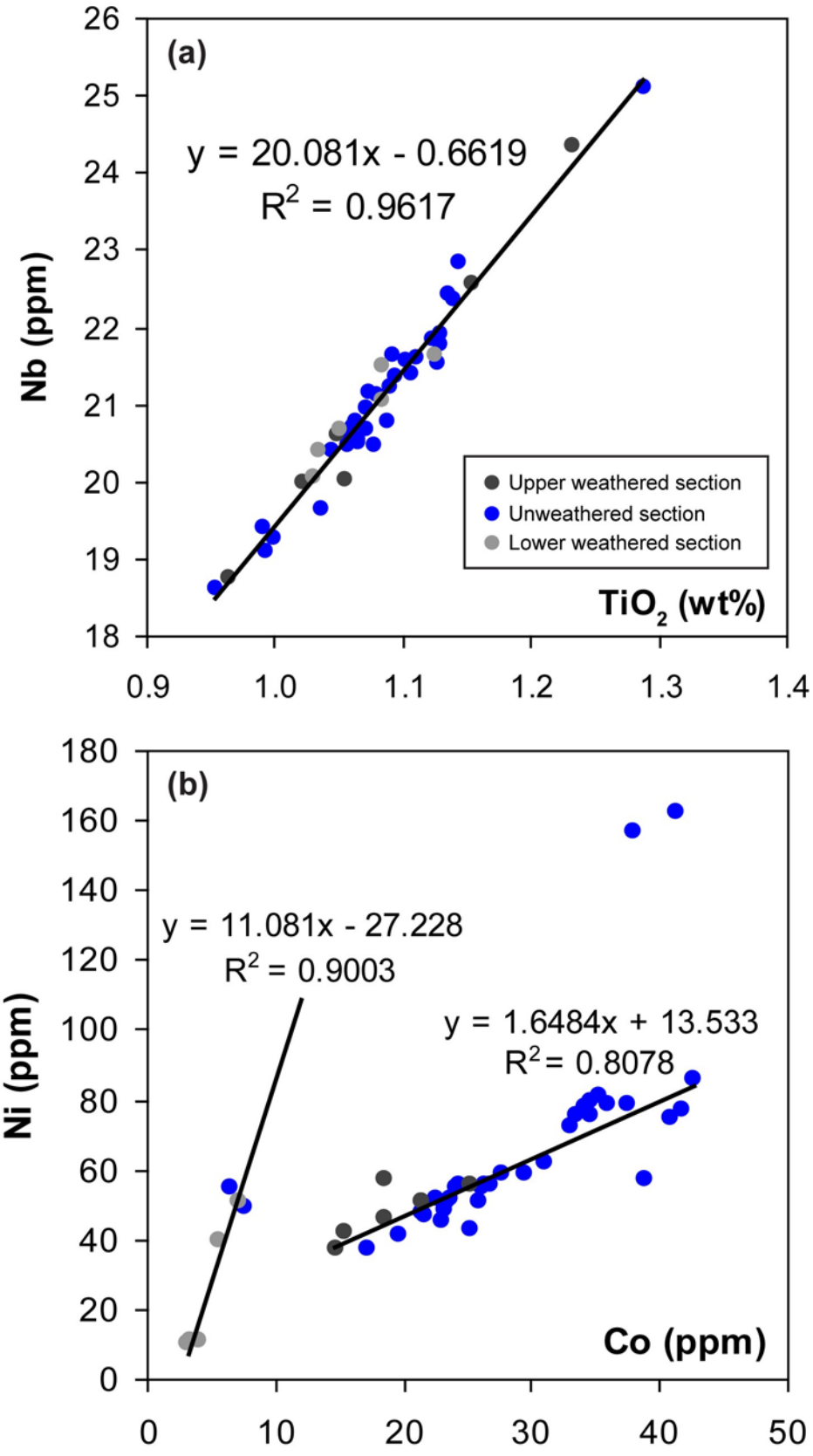
(a)
y = 20.081x - 0.6619
R2 = 0.9617
Upper weathered section
Unweathered section
Lower weathered section
Nb (ppm)
TiO2 (wt%)
26
25
24
23
22
21
20
19
18
0.9
1.0
1.1
1.2
1.3
1.4
(b)
y = 11.081x - 27.228
R2 = 0.9003
y = 1.6484x + 13.533
R2 = 0.8078
Ni (ppm)
Co (ppm)
180
160
140
120
100
80
60
40
20
0
0
10
20
30
40
50

Figure 13

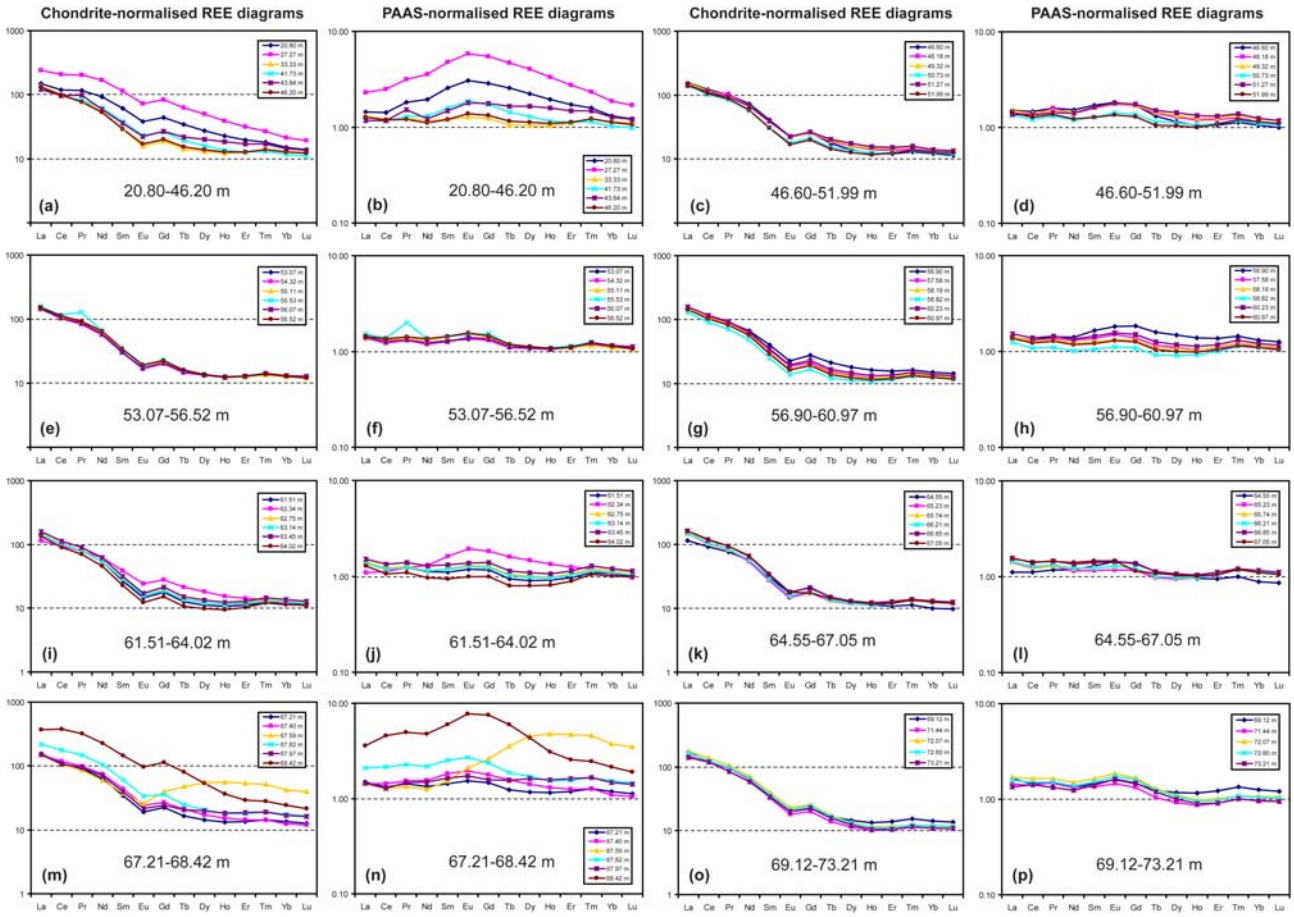
Chondrite-normalised REE diagrams
PAAS-normalised REE diagrams
Chondrite-normalised REE diagrams
PAAS-normalised REE diagrams
(a) 20.80-46.20 m
(b) 20.80-46.20 m
(c) 46.60-51.99 m
(d) 46.60-51.99 m
(e) 53.07-56.52 m
(f) 53.07-56.52 m
(g) 56.90-60.97 m
(h) 56.90-60.97 m
(i) 61.51-64.02 m
(j) 61.51-64.02 m
(k) 64.55-67.05 m
(l) 64.55-67.05 m
(m) 67.21-68.42 m
(n) 67.21-68.42 m
(o) 69.12-73.21 m
(p) 69.12-73.21 m
La Ce Pr Nd Sm Eu Gd Tb Dy Ho Er Tm Yb Lu

Figure 14

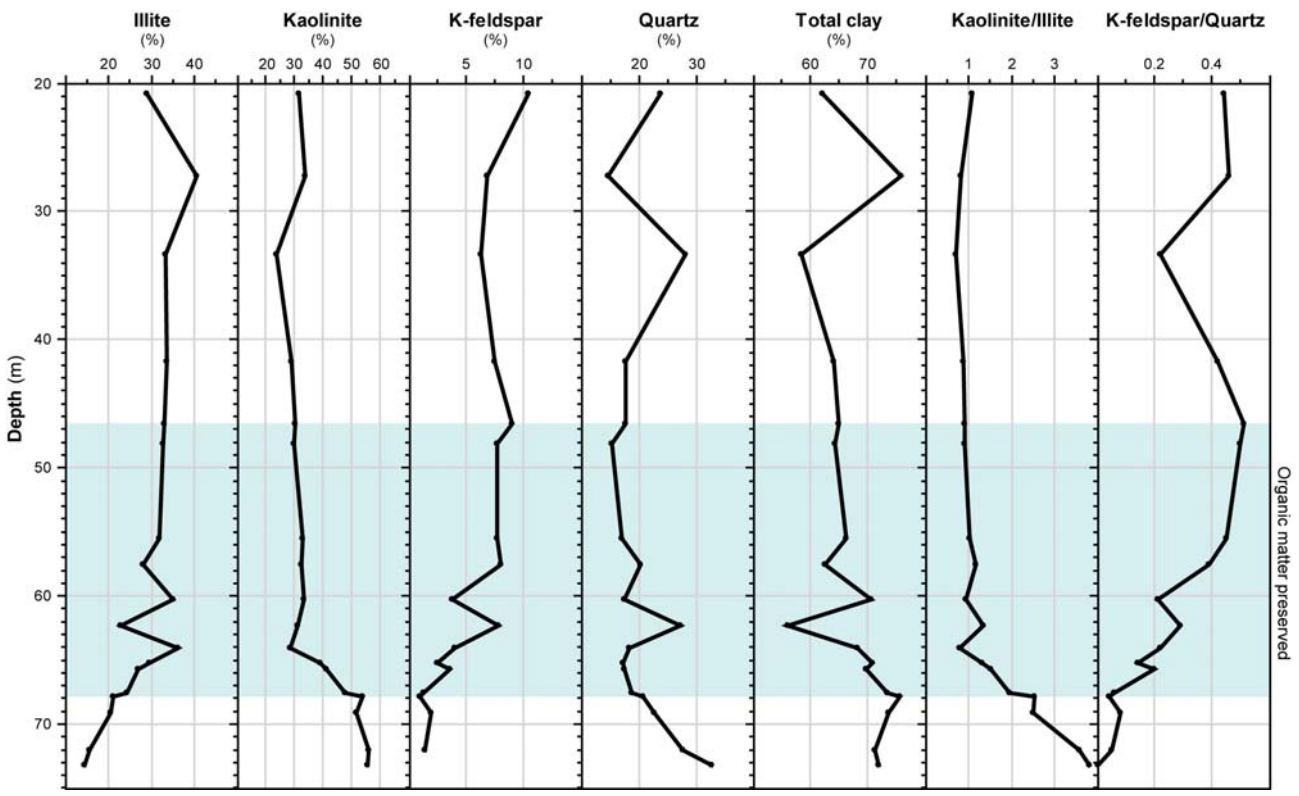
Illite
(%)
20 30 40
Kaolinite
(%)
20 30 40 50 60
K-feldspar
(%)
5 10
Quartz
(%)
20 30
Total clay
(%)
60 70
Kaolinite/Illite
1 2 3
K-feldspar/Quartz
0.2 0.4
Depth (m)
20 30 40 50 60 70
Organic matter preserved

Figure 15

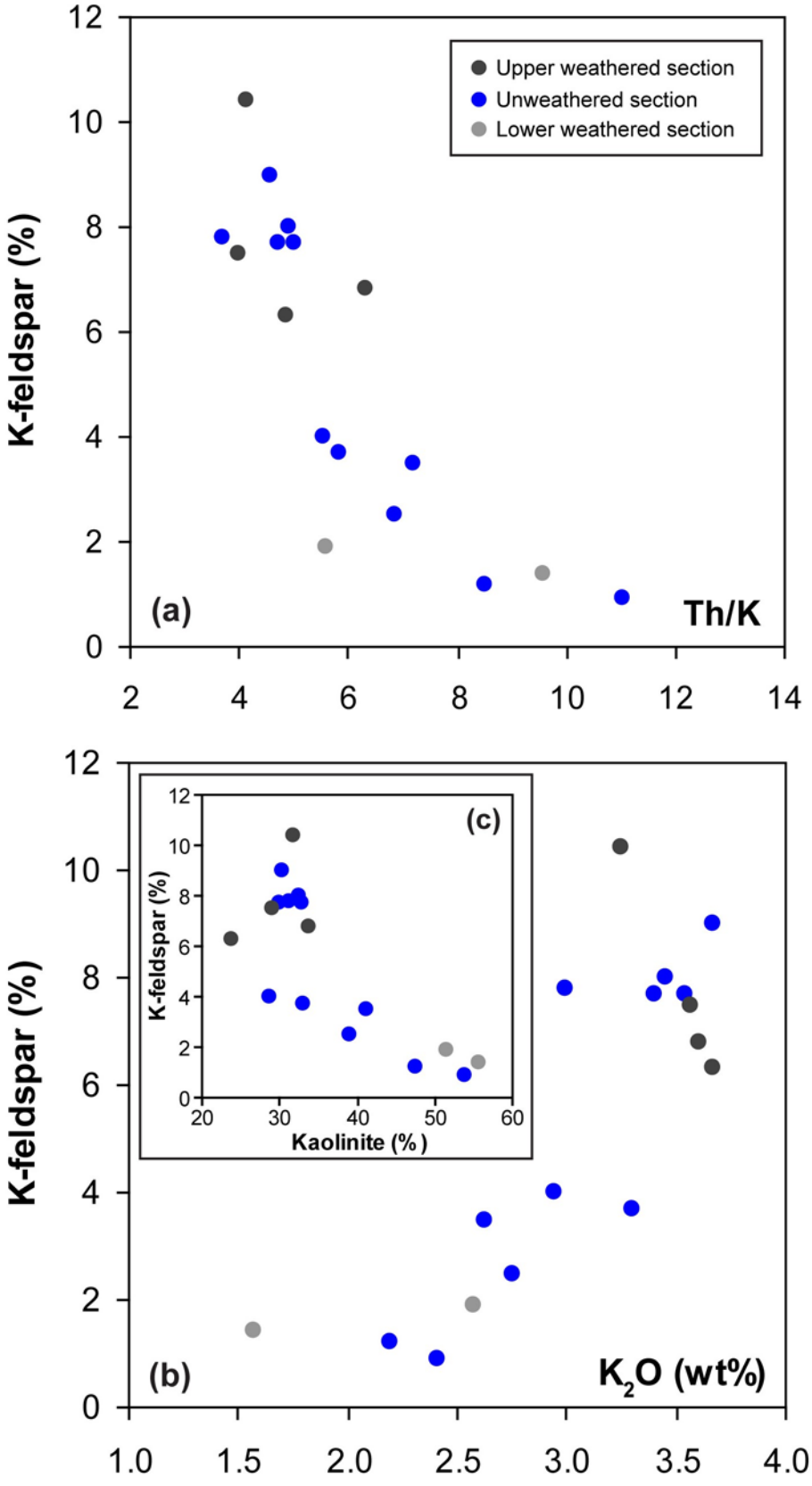
Upper weathered section
Unweathered section
Lower weathered section
K-feldspar (%)
(a)
Th/K
(b)
K2O (wt%)
(c)
Kaolinite (%)

Figure 16

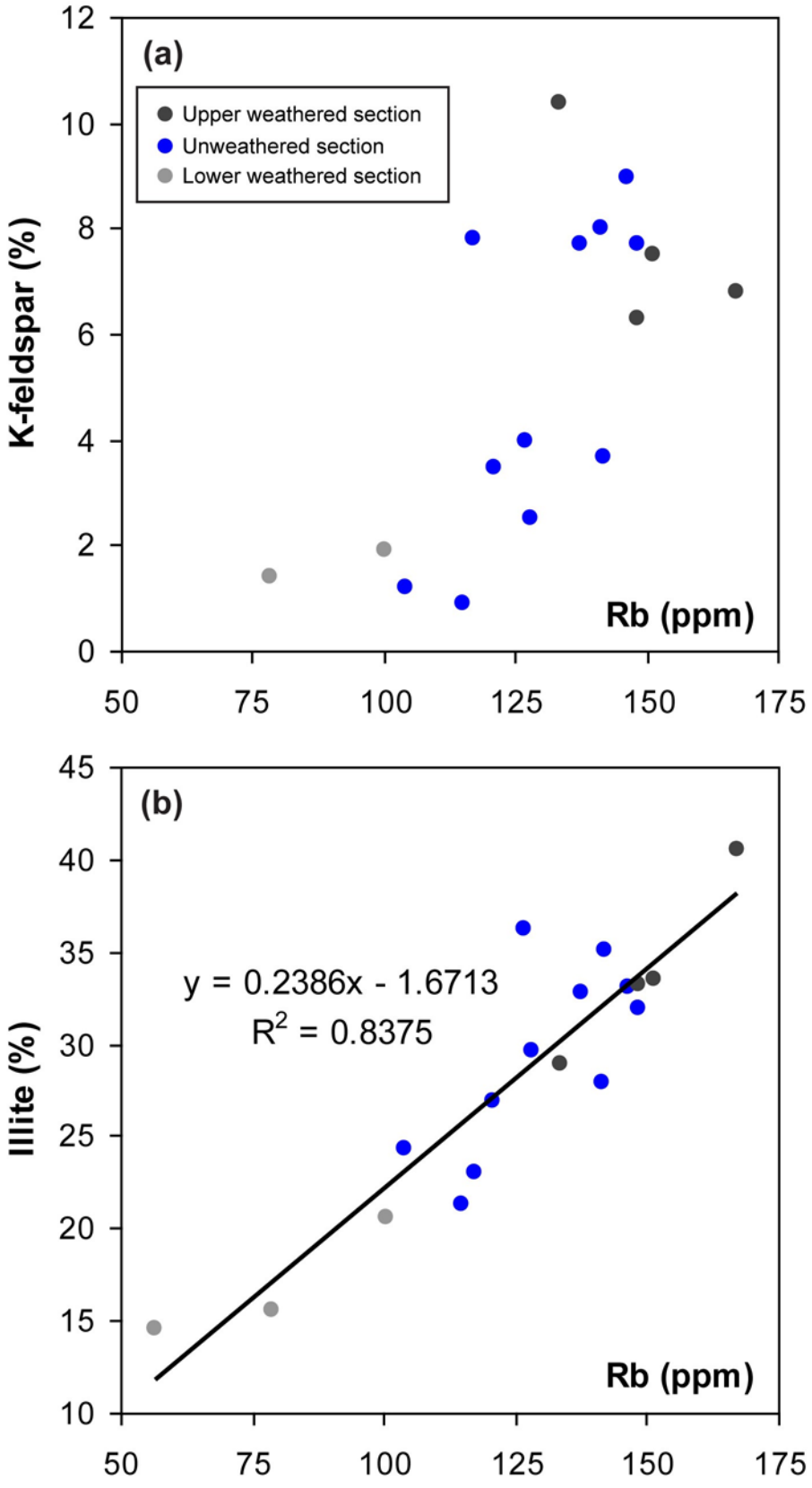
(a)
Upper weathered section
Unweathered section
Lower weathered section
K-feldspar (%)
Rb (ppm)
0
2
4
6
8
10
12
50
75
100
125
150
175
(b)
y = 0.2386x - 1.6713
R2 = 0.8375
Illite (%)
Rb (ppm)
10
15
20
25
30
35
40
45
50
75
100
125
150
175

Figure 17

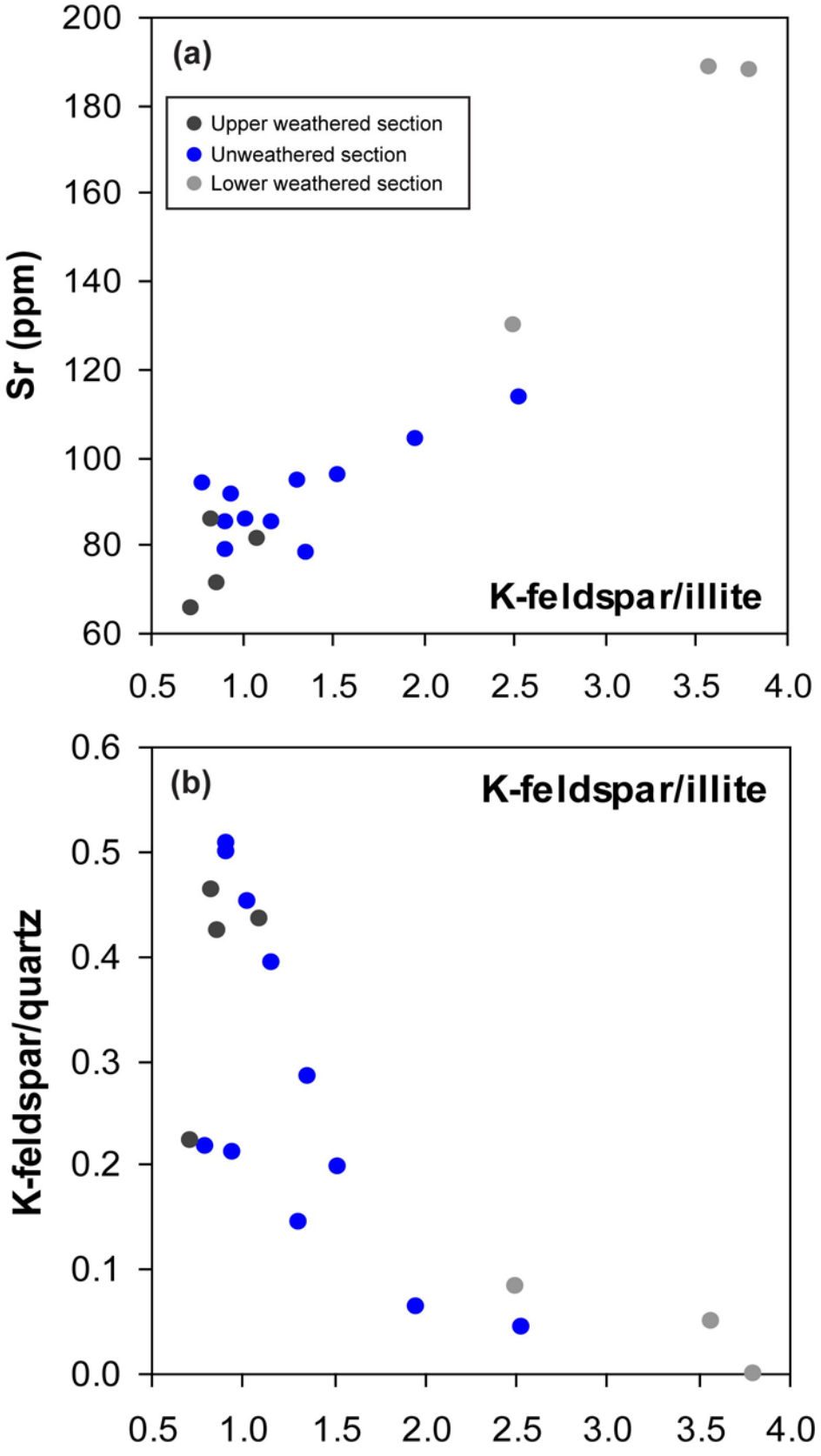
(a)
Upper weathered section
Unweathered section
Lower weathered section
Sr (ppm)
K-feldspar/illite
200
180
160
140
120
100
80
60
0.5
1.0
1.5
2.0
2.5
3.0
3.5
4.0
(b)
K-feldspar/illite
K-feldspar/quartz
0.6
0.5
0.4
0.3
0.2
0.1
0.0

Figure 18